WILEY

An efficient computational approach for three-dimensional modeling and simulation of fibrous battery electrodes

Mohsen Goudarzi[1] | **Davide Grazioli[2]** | **Angelo Simone[2]**

[1]Department of Earth Sciences, Utrecht University, Utrecht, The Netherlands

[2]Department of Industrial Engineering, University of Padova, Padua, Italy

Correspondence
Mohsen Goudarzi, Department of Earth Sciences, Utrecht University, Utrecht, The Netherlands.
Email: m.goudarzi@uu.nl
Davide Grazioli and Angelo Simone, Department of Industrial Engineering, University of Padova, Padua, Italy.
Email: davide.grazioli@unipd.it and angelo.simone@unipd.it

Abstract

Fibrous electrodes are a promising alternative to conventional particle-based lithium-ion battery electrodes. In this contribution, we propose an efficient computational approach for the modeling and simulation of electrochemical phenomena taking place in fibrous electrodes during battery charge/discharge processes. Since each fiber is explicitly modeled by means of a dimensionally reduced embedded fiber model, the framework enables simulations in a three-dimensional setting with relatively modest discretization and computational requirements compared to simulations with fully resolved fiber discretizations. The approach is applied to electrodes with high volume fractions of high aspect ratio fibers. Various local and global quantities are analyzed and results are compared to those obtained with the standard finite element method and the pseudo-2D model.

KEYWORDS

embedded fiber model, fibrous electrode, finite element method, lithium-ion battery electrodes modeling and simulation, nanowire and structural batteries

1 | INTRODUCTION

Fibrous electrodes are appealing alternatives to conventional particle-based electrodes for the next generation of lithium-ion battery systems.[1–4] While fibrous electrodes can be used with a liquid electrolyte solution to enhance electronic conductivity,[5] their properties are better appreciated when embedded in a solid electrolyte in so-called all-solid fibrous electrodes. These solid-state electrodes find application in multifunctional composite materials that can be used for energy harvesting and storage.[6–8] Unlike traditional particle-based electrodes, all-solid fibrous electrodes provide structural strength. This aspect is exploited in structural batteries,[9] a quite recent concept proposed, to the best of our knowledge, by Liu et al.[10] From the modeling perspective, the analysis of fibrous electrodes with classical conformal meshing techniques requires very dense discretizations to describe the fibrous microstructure at the fiber level. Despite the existence of efficient techniques to discretize the microstructure (References 11–17 present some applications of conformal meshing techniques to complex microstructures that can be used in this context), the total memory requirements and solution time may make the calculation prohibitive on a standard desktop computer. To address this issue, we propose an accurate and efficient embedded dimensionally reduced fiber model, to be used in a three-dimensional finite element (FE) method framework, which enables fibrous and electrolyte domains to be discretized independently. Although we

---

Mohsen Goudarzi and Davide Grazioli contributed equally to this work.
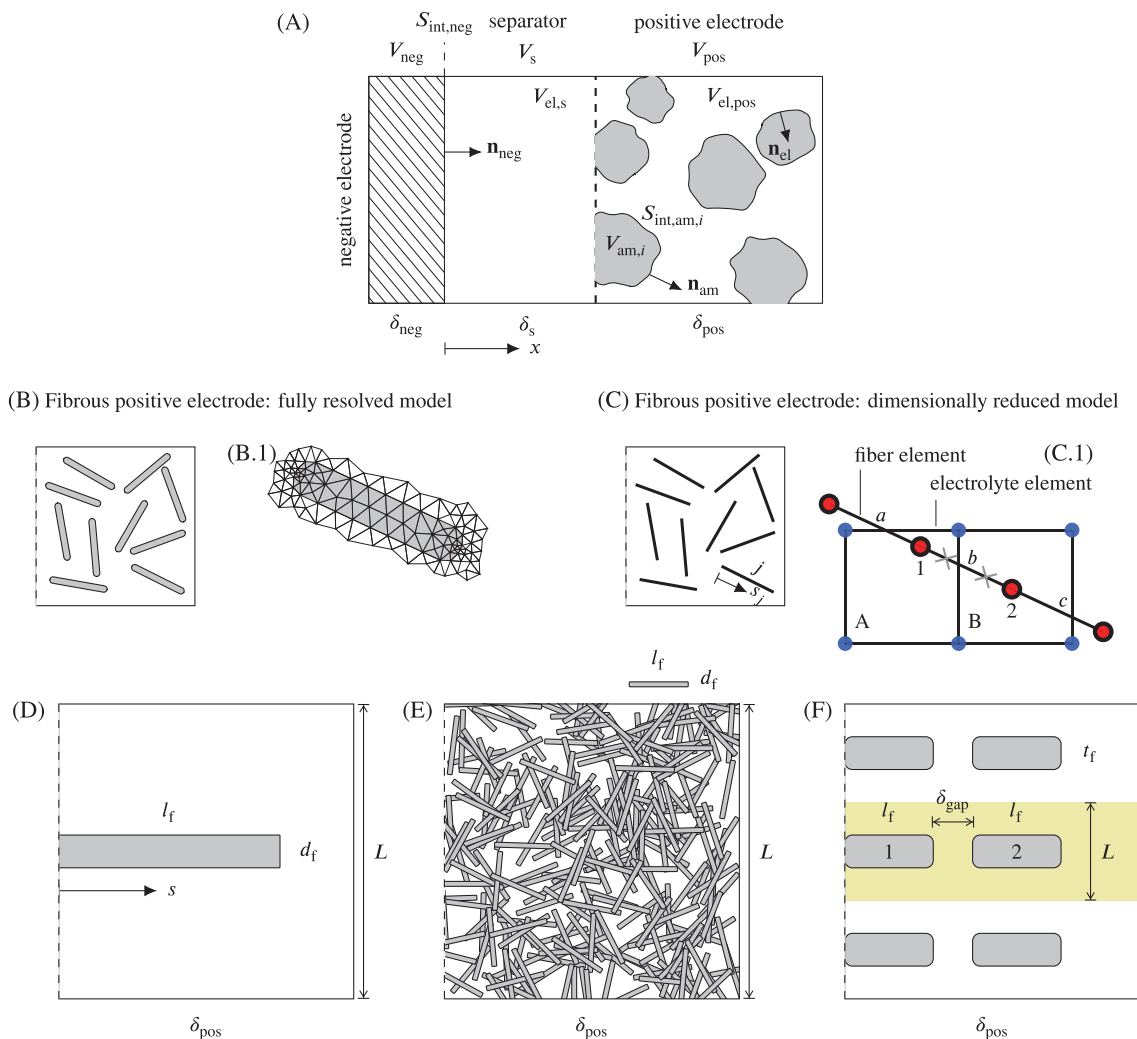

FIGURE 1 (A) Simplified two-dimensional schematic of a lithium-ion battery half cell with a porous positive electrode containing active material inclusions of arbitrary shape in the positive electrode. A fibrous electrode is represented either by means of (B) fully resolved fibers or (C) dimensionally reduced fibers. In panel (C), nodes with the same color share the same set of DOFs (concentration c_{am} and electric potential ϕ_{am} in the fiber in red, concentration c_{el} and electric potential in the electrolyte ϕ_{el} in blue, and the exchanged current $i_{BV,am}$ at the active material-electrolyte interface in black). In panel (C), symbol × indicates the integration points in fiber element b. The bottom row shows the positive electrode configurations analyzed in the example section: (D) single-fiber electrode (Section 5.1); (E) multi-fiber electrode (Section 5.2); and (F) two-fiber electrode (Section 5.3, with the numerical simulations referring to the yellow area)

make reference to the material properties of a polymer electrolyte for comparison purposes, the focus of this work is on the modeling and simulation of fibrous electrodes and not on a specific electrolyte type (liquid or solid).

The battery cell (schematically represented in Figure 1A) is the core structure of batteries: a layered system of a few hundreds micrometers comprising two electrodes and a separator. Upon battery charging and discharging, ions are inserted into or extracted from the active material thanks to electrochemical reactions taking place at the active material-electrolyte interface. The active material content determines the nominal capacity of the cell, while the actual capacity is the result of the interaction between components and the rate of charge/discharge processes. In general, the microstructure of fibrous electrodes is analogous to that of particle-based electrodes. It consists of an agglomerate of fibers, conductive binder, and electrolyte. The latter, for convenience, is represented only in terms of its electrochemical contribution through the governing equations described in Section 2. In the following, we will neglect the conductive binder phase, assuming an electrode consists of discrete fibers embedded in an electrolyte. Such a configuration is known in the literature as one-dimensional electrode architecture, where "one-dimensional" makes reference to the use of fibers, with diameters in the nano- to micron-scale range.

One-dimensional electrode architectures, making use of active material in the shape of fibers (Figure 1, panels (B), (C), and (E)), are of interest for a wide range of applications since they show advantages over traditional design (e.g., particle-based electrodes) in terms of surface area to volume ratio, areal and/or specific capacity, and reduced diffusion

distance between fibers. Multifunctional fibrous electrodes are suitable candidate for wearable electronics[4,18] and structural batteries[6,8,10] thanks to their capability to combine energy storage, mechanical flexibility, and load-bearing functionalities. Furthermore, they are suitable for the development of high-performance battery electrodes.[1–3] Finally, in the light of a battery-based economy that aims at widening the variety of active materials used in batteries (based on lithium-ion chemistry and beyond), nanowire electrode architectures represent an opportunity. Thanks to recent advances in production processes, such as electrospinning, it is nowadays possible to produce low-cost nanofibers from a rich variety of active materials while tuning their spatial arrangement, with basically no limitations on the range of design combinations that can be explored.[1–3, 19, 20]

Despite the progress in computational battery modeling, the numerical simulation of fibrous electrode architectures has lagged behind that of particle-based battery electrodes for many reasons. Compared to particle-based battery electrodes, fibrous electrodes are more difficult to model in an efficient manner because fibers are elongated objects and their representation entails a number of additional design parameters (such as aspect ratio, curvature, spatial orientation). As a consequence, simplified models (such as pseudo-2D models[21]) cannot easily be extended to simulate electrodes with fibrous active material inclusions. To the best of our knowledge, no simplified models are currently available to model fibrous electrodes. This implies that modeling has to follow traditional approaches, using for instance FEM, making simulations like those proposed in this work very costly using mesh conforming techniques.[12,15] This applies in particular to multiscale simulations, where several realizations with the same volume fraction of fibers are necessary to obtain statistically representative information (and before that, a RVE size convergence study has to be conducted). Computational capabilities are currently available for detailed digital representations of battery electrode microstructures and for the simulation of the physical processes taking place within them (refer to the available reviews on the topic for details[22–26]). Nevertheless, the representation of high aspect ratio fibers and the conforming discretization at the fiber-electrolyte interface requires resource intensive mesh generation procedures. Furthermore, the number of fibers that comprise a full-scale electrode with volume fractions typical of porous electrodes (tens of thousands in Section 5.2) eventually results in very large systems of equations that require dedicated computer resources. The modeling studies of Xu et al.[27] and Carlstedt et al.[28] focus on fibrous electrodes with unidirectional fibers. This electrode configuration is amenable for an investigation of the driving processes in a two-dimensional setting, with modest discretization requirements. Such a modeling strategy is however applicable with a limited set of fiber arrangements, as arbitrary electrode configurations dictate the usage of a three-dimensional microstructure representation. The mortar-based approach proposed by Fang et al.[29] represents a step forward towards the reduction of mesh generation costs, as it allows coarse electrolyte FE meshes to be used while employing an appropriate discretization for the active material. Active material particles and electrolyte are discretized using shape-conformal discretizations and non-matching interface nodes, with coupling between them enforced through constraint relations. Although this approach is considerably helpful in many applications, its use for fibrous electrodes with high aspect ratio fibers is practically unfeasible as it could lead to very large system matrices with millions of degrees of freedom (DOFs) even at dilute distributions. A recently proposed approach enables the estimation of the performance of fibrous electrodes by taking into account the geometrical arrangement of the fibers alone.[30] The approach can only be used to determine the nominal electrode capacity as it relies on percolation theory and a simple equivalent resistor network model. Since the actual electrode capacity depends on processes concurrently occurring in different electrode components (such as ionic transport in the electrolyte and solid diffusion in the active materials) and the synergy between them, the electrode response is sensitive to the rate of the process, as discussed in Section 5.2.

To the best of the authors' knowledge, available three-dimensional computational models tailored for fibrous electrodes simulations rely on the lattice Boltzmann's approach and have been developed for redox flow batteries.[31–33] At variance with these approaches, we propose a FE-based dimensionally reduced fiber model ("dimensionally reduced model" from now on) in which the fiber-shaped active material is represented by means of line elements. The approach is derived from recently proposed versions[34,35] of the embedded reinforcement model[36] employed to numerically characterize the mechanical response of fiber-reinforced composite materials. In computational mechanics applications, it is customary to model the fiber-matrix interface through displacement gap-traction force constitutive laws that formally resemble the electrochemical models (e.g., Butler–Volmer equation[37]) describing active materials-electrolyte interactions in battery modeling.[37] Taking advantage of this analogy, the active material-electrolyte coupling is achieved by means of ad-hoc DOFs defined at the interface between a fiber and the electrolyte (Section 4) by making use of two completely independent discretizations for active material and electrode domains. In Section 3, we show that the proposed strategy results in a greatly simplified discretization procedure compared to a traditional fully resolved FE model ("fully resolved model" from now on) as the discretization of one-dimensional active material domains is detached from the three-dimensional discretization of the hosting electrode domain. This is demonstrated in Section 5.2 where we describe the simulations

performed on a three-dimensional fibrous electrode with volume fraction of active material up to 70% (25,000 fibers). The results of the dimensionally reduced model are compared with those obtained with the pseudo-2D model[21] applied on an equivalent porous battery electrode.

Regardless of the large efficiency gain, the modifications required to adapt a standard battery formulation (Section 2) to the proposed dimensionally reduced model are minor (Section 3). This holds true for the numerical implementation too (Section 4). Furthermore, despite the applications of the proposed approach deal with fibers in the micrometer length size range, there are no conceptual limitation to its use for nanowires. As shown in Section 5.1, the only fiber property that controls the correct applicability of the approach is the fiber slenderness, obviously in combination with the set of material parameters. The results indicate that the accuracy of the dimensionally reduced model is comparable with that of fully resolved model starting already at relatively low values of the fiber slenderness. The approach is tested with two sets of governing equations that differ in the electrolyte constitutive model (either based on dilute or concentrated solution theory, Section 2).

2 | GOVERNING EQUATIONS AND WEAK FORM

This section summarizes the governing equations, including the interface conditions that define the interactions between cell/electrode components. The formulation is general and applies to both sets of constitutive equations discussed in this study. The following assumptions are made:

- only lithium-ion battery half cells consisting of homogeneous negative electrode (lithium foil), separator, and composite positive electrode are considered; and
- the positive electrode consists of active material inclusions and the surrounding electrolyte (conductive additives and binder are not explicitly modeled).

Figure 1 shows a schematic representation of the battery cell. The active material inclusions in the positive electrode is hereafter referred to as "active material." Henceforth, subscripts "am," "el," "neg," "pos," and "s" indicate active material, electrolyte, negative and positive electrode, and separator, respectively. According to Figure 1, the active material domain is the union of n_{am} active material inclusions in the positive electrode, that is, $V_{am} = \bigcup_{i=1}^{n_{am}} V_{am,i}$, and the same holds for the active material-electrolyte interface $S_{int,am} = \bigcup_{i=1}^{n_{am}} S_{int,am,i}$. The electrolyte domain is defined accordingly as $V_{el} = V_{el,s} \cup V_{el,pos}$ where $V_{el,s} = V_s$ and $V_{pos} = V_{am} \cup V_{el,pos}$, with $V_{am} \cap V_{el,pos} = \emptyset$. The identification of negative electrode domain V_{neg} and negative electrode-electrolyte interface $S_{int,neg}$ is straightforward.

2.1 | Balance equations

The problem is formulated in terms of molar concentration c (number of moles per unit volume) and electric potential ϕ in the negative electrode, electrolyte, and active material of the positive electrode. Mass and charge balance in each of these domains are assumed to obey relations

$$\frac{\partial c_k}{\partial t} + \operatorname{div} \mathbf{h}_k = 0, \quad \mathbf{x} \in V_k, \ t \in (0, t_{end}), \quad \text{and} \tag{1a}$$

$$\operatorname{div} \mathbf{i}_k = 0, \quad \mathbf{x} \in V_k, \ t \in (0, t_{end}), \tag{1b}$$

respectively, with k = neg, el, and am. Vectors $\mathbf{h}$ and $\mathbf{i}$ represent the mass flux (number of moles per unit time per unit area), and the electric current density (electric charge per unit time per unit area), respectively, while V_k is the domain the equation refers to.

2.2 | Interface conditions

Continuity of the electric current density across the interface S_{int} between electrolyte and electrode material is enforced through

$$\mathbf{i}_{neg} \cdot \mathbf{n}_{neg} = -\mathbf{i}_{el} \cdot \mathbf{n}_{el} = i_{BV,neg}, \quad \mathbf{x} \in S_{int,neg}, \ t \in (0, t_{end}), \quad \text{and} \tag{2a}$$

$$\mathbf{i}_{am} \cdot \mathbf{n}_{am} = -\mathbf{i}_{el} \cdot \mathbf{n}_{el} = i_{BV,am}, \quad \mathbf{x} \in S_{int,am}, \ t \in (0, t_{end}), \tag{2b}$$

where $\mathbf{n}_{neg}$, $\mathbf{n}_{el}$, and $\mathbf{n}_{am}$ are the outward unit normals with respect to the negative electrode, electrolyte, and active material inclusions domains, respectively. The relationships $\mathbf{n}_{el} = -\mathbf{n}_{neg}$, and $\mathbf{n}_{el} = -\mathbf{n}_{am}$ hold on interfaces $S_{int,neg}$ and $S_{int,am}$, respectively. The term i_{BV} quantifies the charge transfer across the interface and, according to Faraday's law, is related to lithium transfer through

$$\mathbf{h}_{neg} \cdot \mathbf{n}_{neg} = -\frac{1}{\alpha_{BV}} \mathbf{h}_{el} \cdot \mathbf{n}_{el} = \frac{1}{F} i_{BV,neg}, \quad \mathbf{x} \in S_{int,neg}, \ t \in (0, t_{end}), \quad \text{and} \tag{3a}$$

$$\mathbf{h}_{am} \cdot \mathbf{n}_{am} = -\frac{1}{\alpha_{BV}} \mathbf{h}_{el} \cdot \mathbf{n}_{el} = \frac{1}{F} i_{BV,am}, \quad \mathbf{x} \in S_{int,am}, \ t \in (0, t_{end}), \tag{3b}$$

where F is Faraday's constant. Coefficient α_{BV} takes different values depending on the constitutive model used for the electrolyte: $\alpha_{BV} = D_{X^-}/(D_{Li^+} + D_{X^-})$ is consistent with the formulation described in Table 1 (refer to Section 3 of Reference 38 for the derivation); $\alpha_{BV} = 1$ is consistent with Doyle's formulation described in Table 2.

The charge transfer i_{BV} is usually related to the values of the field variables at the two sides of the interface through equations that describe the electrochemical reaction. For the sake of generality, we express this relationship as

$$i_{BV} = f_{BV}(\phi_{am}, \phi_{el}, c_{am}, c_{el}), \quad \mathbf{x} \in S_{int}, \ t \in (0, t_{end}), \tag{4}$$

where f_{BV} is a known function of field variables at the interface. Refer to Tables 1, 2, and 4 for explicit expressions of f_{BV} at interfaces $S_{int,neg}$ and $S_{int,am}$.

2.3 | Constitutive equations

The dimensionally reduced approach is applicable irrespective of the constitutive models employed. We perform numerical simulations with two formulations that differ in (i) constitutive equations for the electrolyte and (ii) constitutive equations of the charge transfer across the interfaces between electrolyte and electrode materials. Distinctive features are summarized in Tables 1 and 2. The first formulation (Table 1) makes use of dilute solution theory (Equations 5 and 6) and linearized Butler–Volmer equation (Equations 7 and 8). The second formulation (Table 2) makes use of concentrated solution theory (Equations 9 and 10) and exponential Butler–Volmer equation (Equations 12 and 13).

TABLE 1 Constitutive equations for electrolyte and interfaces: Dilute solution theory and linearized Butler–Volmer equation

Domain	Definition	Expression	Equation
V_{el}	Apparent mass flux[a]	$\mathbf{h}_{el} = -D_{el} \nabla c_{el}$	(5)
	Electric current density[a]	$\mathbf{i}_{el} = \gamma_c \nabla c_{el} - \gamma_\phi c_{el} \nabla \phi_{el}$	(6)
	Apparent diffusivity	$D_{el} = \frac{2\, D_{Li^+}\, D_{X^-}}{D_{Li^+} + D_{X^-}}$	
	Diffusion contribution coefficient	$\gamma_c = F\,(D_{X^-} - D_{Li^+})$	
	Migration contribution coefficient	$\gamma_\phi = \frac{F^2}{R\,T}\,(D_{Li^+} + D_{X^-})$	
$S_{int,neg}$	Charge transfer[b]	$f_{BV,neg} = i_{0,neg}\, \frac{F}{RT} \eta_{neg}$	(7)
$S_{int,am}$	Charge transfer[b]	$f_{BV,am} = i_{0,am}\, \frac{F}{RT} \eta_{am}$	(8)
α_{BV}	Interface coefficient	$\alpha_{BV} = \frac{D_{X^-}}{D_{Li^+} + D_{X^-}}$	

Note: Material parameters are listed in Tables 4 and 5.
[a]Formulation based on dilute solution theory. Details about the derivation of the constitutive equations can be found, for example, in References 38 and 39.
[b]Surface overpotential η_k, with $k =$ neg, am, defined in (14).

The formulations entail the same basic ingredients. The sources of nonlinearities lie both in electrolyte constitutive models (notice the second term at the right-hand side of (6) and (10)) and in the definition of the charge transfer f_{BV}.

TABLE 2 Constitutive equations for electrolyte and interfaces: Concentrated solution theory and exponential Butler–Volmer equation

Domain	Definition	Expression	Equation
V_{el}	Mass flux	$\mathbf{h}_{el} = -D_{el}\,\nabla c_{el} + \frac{t_{el}}{F}\mathbf{i}_{el}$	(9)
	Electric current density	$\mathbf{i}_{el} = -\kappa_{el}\,\nabla\phi_{el} + \kappa_D\,\nabla\ln c_{el}$	(10)
	Diffusional conductivity	$\kappa_D = \frac{2RT}{F}\kappa_{el}\left(1 + \frac{\partial\ln f_{el}}{\partial\ln c_{el}}\right)(1 - t_{el})$	(11)
$S_{int,neg}$	Charge transfer[a]	$f_{BV,neg} = i_{0,neg}\left(\exp\left(\frac{\alpha_a F}{RT}\eta_{neg}\right) - \exp\left(-\frac{\alpha_c F}{RT}\eta_{neg}\right)\right)$	(12)
$S_{int,am}$	Charge transfer[a]	$f_{BV,am} = i_{0,am}\left(\exp\left(\frac{\alpha_a F}{RT}\eta_{am}\right) - \exp\left(-\frac{\alpha_c F}{RT}\eta_{am}\right)\right)$	(13)
α_{BV}	Interface coefficient	$\alpha_{BV} = 1$	

Note: Formulation equivalent to that used by Doyle et al.[21] Material parameters are listed in Tables 4 and 6.
[a]Surface overpotential η_k, with k = neg, am, defined in (14).

Terms $i_{0,neg}$ and $i_{0,am}$ (in (7), (8), (12), and (13)) depend nonlinearly on concentrations c_{el} and c_{am} (Table 4), and the surface overpotential

$$\eta_k = \phi_k - \phi_{el} - U_{OC,k}, \quad \mathbf{x} \in S_{int,k}, \quad \text{with } k = \text{neg, am,} \tag{14}$$

adds nonlinearities through the dependence of the open circuit potential U_{OC} on concentration c_{am} (Table 4). An additional source of nonlinearity in the formulation presented in Table 2 is given by the dependence of terms κ_{el} and t_{el} on concentration c_{el} (Table 6).

The constitutive equations for negative electrode and active material inclusions in the positive electrode are the same for all the numerical examples and are listed in Table 3. Fick's law describes the mass flux (Equations 15 and 17), and Ohm's law describes the electric current density in the active material (Equations 16 and 18).

TABLE 3 Constitutive equations for negative electrode and active material inclusions

Domain	Definition	Expression	Equation
V_{neg}	Mass flux	$\mathbf{h}_{neg} = -D_{neg}\nabla c_{neg}$	(15)
	Electric current density	$\mathbf{i}_{neg} = -\kappa_{neg}\nabla\phi_{neg}$	(16)
V_{am}	Mass flux	$\mathbf{h}_{am} = -D_{am}\nabla c_{am}$	(17)
	Electric current density	$\mathbf{i}_{am} = -\kappa_{am}\nabla\phi_{am}$	(18)

Note: Material parameters are listed in Table 4.

2.4 | Boundary conditions

We exclusively simulate galvanostatic discharge processes. To this end, we apply boundary conditions

$$\mathbf{i}_{neg}\cdot\mathbf{n}_{neg} = -I, \quad x = -\delta_{neg} \quad \text{and} \tag{19a}$$
$$\mathbf{h}_{neg}\cdot\mathbf{n}_{neg} = 0, \quad x = -\delta_{neg} \tag{19b}$$

at the left-hand edge of the negative electrode (at $x = -\delta_{neg}$, with reference to the choice of the coordinate system in Figure 1), where $\mathbf{n}_{neg}$ is the outward unit normal with respect to the negative electrode. According to (19a), a positive value of I represents a discharge process, that is, lithium is extracted from the lithium foil and is inserted into the active material of the positive electrode.

In the positive electrode, we assume there exists a fictitious electronic conductive network that is superimposed to the active material inclusions: the network keeps the active material inclusions at the same electric potential, and no lithium exchange occurs between it and the active material. For convenience, we set

$$\phi_{am} = 0, \quad \forall x \in [\delta_s, \delta_s + \delta_{pos}], \tag{20}$$

which means that (18) does not actually come into play. A similar approach was followed, for example, by Carlstedt et al.[28] In practical applications, the condition of equipotential active material can be approached if: (i) conductive additives in the electrode form an extended conductive network that links the whole active material to the current collector; (ii) a perfect active material-conductive additive adhesion is attained all-over the electrode; and (iii) the electronic conductivity of the additives is sufficiently high to make the potential losses in the conductive network negligible. For simplicity, we assume that all these conditions are met in the fibrous electrodes under consideration.

The explicit representation and modeling of conductive additive-polymer binder mixture is desirable for porous electrode design optimization,[11,13,40] but it is beyond the scope of this contribution. An intermediate approach (between setting (20) and the direct representation) would be to model the binder mixture as an homogenized matrix surrounding the fibers (refer, e.g., to References 14 and 41, among many others). With reference to this last option, our choice (20) is consistent with the material parameters reported by Doyle et al.[21] (i.e., the reference used for the numerical simulation setup in Section 5), who make use of a homogenized electrical conductivity of the positive electrode $\kappa_{\mathrm{pos}} = 10^4$ S m^{-1} (σ in the reference). From the rough estimate $\Delta\phi_{\mathrm{pos}} \sim I\,\delta_{\mathrm{pos}}/\kappa_{\mathrm{pos}}$, the potential drop across the entire positive electrode is in the order of 10^{-7} V with an electrode of thickness $\delta_{\mathrm{pos}} = 100$ μm (refer to Section 5.2) and boundary condition (19a) set to $I = 10$ A m^{-2} (the largest current density considered in our numerical simulations). Setting the electric potential to all fibers according to (20) appears a reasonable option in this study.

2.5 | Initial conditions

A uniform concentration of lithium at $t = 0$ according to

$$c_{\mathrm{neg}} = c_{\mathrm{neg}}^0, \quad \mathbf{x} \in V_{\mathrm{neg}}, \ t = 0, \tag{21a}$$

$$c_{\mathrm{el}} = c_{\mathrm{el}}^0, \quad \mathbf{x} \in V_{\mathrm{el}}, \ t = 0, \tag{21b}$$

$$c_{\mathrm{am}} = c_{\mathrm{am}}^0, \quad \mathbf{x} \in V_{\mathrm{am}}, \ t = 0, \tag{21c}$$

is assumed inside each cell component, where c_{el}^0, c_{am}^0, and c_{neg}^0 are initial concentration values. As long as no current flows through the cell, equilibrium conditions hold and the electric potential is uniform within each cell constituent. Since conditions $i_{\mathrm{BV,neg}} = i_{\mathrm{BV,am}} = 0$ hold too, both couples of definitions (7)–(8) and (12)–(13) lead to $\eta_{\mathrm{neg}} = \eta_{\mathrm{am}} = 0$ (c_{el}^0 and c_{am}^0 are set so that electric current densities $i_{0,\mathrm{neg}}$ and $i_{0,\mathrm{am}}$ are nonzero at $t = 0$). The initial potential values are thus

$$\phi_{\mathrm{neg}} = U_{\mathrm{OC,neg}} - U_{\mathrm{OC,am}}, \quad \mathbf{x} \in V_{\mathrm{neg}}, \ t = 0, \tag{22a}$$

$$\phi_{\mathrm{el}} = -U_{\mathrm{OC,am}}, \quad \mathbf{x} \in V_{\mathrm{el}}, \ t = 0, \tag{22b}$$

according to (14), if

$$\phi_{\mathrm{am}} = 0, \quad \mathbf{x} \in V_{\mathrm{am}}, \ t = 0 \tag{22c}$$

is set in agreement with boundary condition (20).

2.6 | Weak form

Following a standard Galerkin approach, the weak forms of the balance equations for negative electrode, electrolyte, and active material inclusions can be obtained. Equation (4) is weakly enforced on each interface $S_{\mathrm{int,neg}}$ and $S_{\mathrm{int,am}}$ through

$$\int_{S_{\mathrm{int,neg}}} \hat{\imath}_{\mathrm{BV,neg}} \left(i_{\mathrm{BV,neg}} - f_{\mathrm{BV,neg}} \left(\phi_{\mathrm{neg}}, \phi_{\mathrm{el}}, c_{\mathrm{neg}}, c_{\mathrm{el}} \right) \right) \ \mathrm{d}S = 0, \tag{23a}$$

$$\int_{S_{\mathrm{int,am}}} \hat{\imath}_{\mathrm{BV,am}} \left(i_{\mathrm{BV,am}} - f_{\mathrm{BV,am}} \left(\phi_{\mathrm{am}}, \phi_{\mathrm{el}}, c_{\mathrm{am}}, c_{\mathrm{el}} \right) \right) \ \mathrm{d}S = 0, \tag{23b}$$

for each admissible test function $\hat{\imath}_{BV,neg}$ restricted to $S_{int,neg}$ and each $\hat{\imath}_{BV,am}$ restricted to $S_{int,am}$. The weak forms resulting from (1) over V_{neg} and V_{am} read

$$-\int_{V_{neg}} \nabla\hat{\phi}_{neg} \cdot \mathbf{i}_{neg} \ dV + \int_{S_{int,neg}} \hat{\phi}_{neg} \ i_{BV,neg} \ dS = 0, \tag{24a}$$

$$\int_{V_{neg}} \hat{c}_{neg} \frac{\partial c_{neg}}{\partial t} \ dV - \int_{V_{neg}} \nabla\hat{c}_{neg} \cdot \mathbf{h}_{neg} \ dV + \frac{1}{F}\int_{S_{int,neg}} \hat{c}_{neg} \ i_{BV,neg} \ dS = 0, \tag{24b}$$

and

$$-\int_{V_{am}} \nabla\hat{\phi}_{am} \cdot \mathbf{i}_{am} \ dV + \int_{S_{int,am}} \hat{\phi}_{am} \ i_{BV,am} \ dS = 0, \tag{25a}$$

$$\int_{V_{am}} \hat{c}_{am} \frac{\partial c_{am}}{\partial t} \ dV - \int_{V_{am}} \nabla\hat{c}_{am} \cdot \mathbf{h}_{am} \ dV + \frac{1}{F}\int_{S_{int,am}} \hat{c}_{am} \ i_{BV,am} \ dS = 0, \tag{25b}$$

respectively, for every admissible test functions $\hat{\phi}_{neg}$, $\hat{c}_{neg}$, $\hat{\phi}_{am}$, and $\hat{c}_{am}$. Analogously, the weak forms over V_{el} read

$$-\int_{V_{el}} \nabla\hat{\phi}_{el} \cdot \mathbf{i}_{el} \ dV - \int_{S_{int,neg}} \hat{\phi}_{el} \ i_{BV,neg} \ dS - \int_{S_{int,am}} \hat{\phi}_{el} \ i_{BV,am} \ dS = 0, \tag{26a}$$

$$\int_{V_{el}} \hat{c}_{el} \frac{\partial c_{el}}{\partial t} \ dV - \int_{V_{el}} \nabla\hat{c}_{el} \cdot \mathbf{h}_{el} \ dV - \frac{\alpha_{BV}}{F}\int_{S_{int,neg}} \hat{c}_{el} \ i_{BV,neg} \ dS - \frac{\alpha_{BV}}{F}\int_{S_{int,am}} \hat{c}_{el} \ i_{BV,am} \ dS = 0, \tag{26b}$$

for every admissible test functions $\hat{\phi}_{el}$ and $\hat{c}_{el}$, respectively. The functions to be integrated over interfaces $S_{int,neg}$ and $S_{int,am}$ in (24), (25), and (26) result from (2), (3), (4), and (23), respectively.

3 | DIMENSIONALLY REDUCED MODEL

A fully resolved representation of the electrode components of the type represented in Figure 1B makes the numerical solution of the weak form (23)–(26) extremely demanding when electrodes consist of high aspect ratio active fibers.[1–4,6,8,18] To overcome this limitation, we introduce a dimensionally reduced model tailored for fiber-shaped active materials (Figure 1C). Inspired by embedded reinforcement models used in computational mechanics for the simulation of fiber-reinforced composites,[36] we represent active fibers as one-dimensional objects (i.e., straight lines in this study) whose discretization is independent of that of the electrolyte and consists of conventional linear one-dimensional Lagrange elements in both two- and three-dimensions. Figure 1C.1 shows the case of two electrolyte elements crossed by a dimensionally reduced fiber discretized with three linear elements. The independence of the two discretizations is evident: the nodes of the fiber elements (in red) do not coincide with the intersection points between fiber axis and electrolyte elements' edges (the nodes of the electrolyte elements are drawn in blue). While any fiber discretization can be used, in the numerical simulations fiber nodes are uniformly distributed for convenience. Most importantly, there are no limitations on the number of fibers that can cross an electrolyte element. The fiber-electrolyte mesh-conformity restriction (Figure 1B.1), proper of most fully resolved models, is therefore removed, making the fully independent discretization of fibers and electrolyte domains possible. Finally, the connection between fibers and electrolyte is dealt with through appropriate interface contributions. These contributions are conveniently discretized in a conforming manner along the fibers (in Figure 1C the nodes of the fiber elements, in red, coincide with those of the interface in black).

Dimensional reduction of active fibers

The representation of a fiber as a one-dimensional object rests upon the following assumption: on an arbitrary cross-section perpendicular to the fiber axis ("fiber cross-section" from now on) the ratio between the value of a field variable at an arbitrary point on the cross section and the average cross-sectional value approaches one. Therefore, a single value of ϕ_{am}, c_{am}, and $i_{BV,am}$ is associated at coordinate s along the fiber axis.

The validity of this assumption cannot be postulated beforehand because it depends on the combination of several factors (fiber diameter and charge/discharge rate among others). Radial concentration gradients have been experimentally detected by Jacques et al.[42] in carbon fibers undergoing charge/discharge. A relationship between the slope of the gradient and the charge/discharge rate was foreseen and later confirmed by the numerical study of Xu et al.[27] The latter also show that modest radial concentration gradients develop with a wide range of fiber diffusion coefficients (D_{am} between 10^{-14} and 10^{-11} m^2 s^{-1}) at low rates (1 C), but significant concentration gradients only develop with low diffusion coefficient ($D_{am} = 10^{-14}$ m^2 s^{-1}) at higher rates (10 C). In order to explore the range of applicability of the dimensionally reduced model, the results of the dimensionally reduced and fully resolved models are compared in Section 5.1 for various fiber geometrical features and discharge rates.

In the reminder of this section, we focus on weak forms (23b), (25), and (26), as the negative electrode is handled in a standard fashion. In the fibrous electrode under consideration, n_{am} indicates the number of fibers and the porosity $\epsilon = V_{el,pos}/V_{pos} = 1 - V_{am}/V_{pos}$ quantifies the electrolyte volume fraction in the positive electrode (Figure 1A), assumed to be uniform in space and constant in time. The formulation presented in this section applies whenever fibers can be represented as generalized cylinders of constant cross-section. For convenience, we consider right circular cylinders of diameter d_j and length l_j (Figures 1A,C) so that each jth fiber has volume $V_{am,j} = \pi d_j^2 l_j/4$. Under these assumptions, weak forms (25) and (23b) are recast as

$$- A_j \int_{l_j} \frac{\partial \hat{\phi}_{am}}{\partial s_j} \, i_{am} \, ds_j + C_j \int_{l_j} \hat{\phi}_{am} \, i_{BV,am} \, ds_j = 0, \quad \forall j = 1, \ldots, n_{am}, \tag{27a}$$

$$A_j \int_{l_j} \hat{c}_{am} \frac{\partial c_{am}}{\partial t} \, ds_j - A_j \int_{l_j} \frac{\partial \hat{c}_{am}}{\partial s_j} \, h_{am} \, ds_j + \frac{C_j}{F} \int_{l_j} \hat{c}_{am} \, i_{BV,am} \, ds_j = 0, \quad \forall j = 1, \ldots, n_{am}, \tag{27b}$$

and

$$C_j \int_{l_j} \hat{i}_{BV,am} \left(i_{BV,am} - f_{BV,am} \left(\phi_{am}, \phi_{el}, c_{am}, c_{el} \right) \right) \, ds_j = 0, \quad \forall j = 1, \ldots, n_{am}, \tag{28}$$

respectively, being $s_j \in [0, l_j]$ the one-dimensional coordinate defined along the axis of the jth fiber (Figure 1C). Electric current density i_{am} and mass flux h_{am} are indicated without boldface to emphasize their one-dimensional nature in this modeling approach. Details about the mapping between the local coordinate s_j and the global coordinate $\mathbf{x} \in V_{pos}$ are provided in Section 4.1. Scalars A_j and C_j are the cross-sectional area and the circumference of the jth fiber, respectively. For simplicity, we neglect the contributions of fiber circular edges, so that $S_{int_j} = C_j \, l_j$. In Section 5.1, we show that the implications of this simplification are negligible for high aspect ratio fibers.

The integration over the electrolyte V_{el} is split into separator V_s and positive electrode V_{pos} domains. In the positive electrode, it is convenient to perform the integration of (26) over the volume V_{pos} and correct the integrals through porosity ϵ to cancel out the contribution of the volume occupied by the fiber:

$$- \int_{V_s} \nabla \hat{\phi}_{el} \cdot \mathbf{i}_{el} \, dV - \epsilon \int_{V_{pos}} \nabla \hat{\phi}_{el} \cdot \mathbf{i}_{el} \, dV - \int_{S_{int,neg}} \hat{\phi}_{el} \, i_{BV,neg} \, dS - \sum_{j=1}^{n_{am}} C_j \int_{l_j} \hat{\phi}_{el} \, i_{BV,am} \, ds_j = 0, \tag{29a}$$

$$\int_{V_s} \hat{c}_{el} \frac{\partial c_{el}}{\partial t} \, dV + \epsilon \int_{V_{pos}} \hat{c}_{el} \frac{\partial c_{el}}{\partial t} \, dV - \int_{V_s} \nabla \hat{c}_{el} \cdot \mathbf{h}_{el} \, dV - \epsilon \int_{V_{pos}} \nabla \hat{c}_{el} \cdot \mathbf{h}_{el} \, dV$$

$$- \frac{\alpha_{BV}}{F} \int_{S_{int,neg}} \hat{c}_{el} \, i_{BV,neg} \, dS - \sum_{j=1}^{n_{am}} \frac{C_j \, \alpha_{BV}}{F} \int_{l_j} \hat{c}_{el} \, i_{BV,am} \, ds_j = 0 . \tag{29b}$$

At the interface between the separator and the positive electrode at $x = \delta_s$ (Figure 1A) continuity of field variables c_{el} and ϕ_{el} holds together with conditions

$$\left(\mathbf{h}_{el}|_{\mathbf{x} \in V_s} - \epsilon \, \mathbf{h}_{el}|_{\mathbf{x} \in V_{pos}} \right) \cdot \mathbf{n}_s = 0, \quad \text{and} \quad \left(\mathbf{i}_{el}|_{\mathbf{x} \in V_s} - \epsilon \, \mathbf{i}_{el}|_{\mathbf{x} \in V_{pos}} \right) \cdot \mathbf{n}_s = 0.$$

By performing the numerical integration over the total volume V_{pos}, rather than the actual electrolyte volume $V_{el,pos}$, a significant operative simplification is introduced (Figure 1A clarifies the relationship between V_{pos} and $V_{el,pos}$): the

discretizations of electrolyte domain and fibers and their geometrical representations do not have to be conforming. The implications of this simplification are those commonly encountered in established battery modeling approaches. Equation (29) presents several analogies with the treatment of the pore-filling electrolyte typical of porous electrode theory.[43] For example, concentrations c_{el} and $\epsilon\, c_{\text{el}}$ are equivalent to the "solution-phase concentration" and the "superficial concentration, averaged over the volume of both matrix and pores" defined in Reference 43, respectively. Similarly, terms $\mathbf{h}_{\text{el}}$ and $\epsilon\, \mathbf{h}_{\text{el}}$ are equivalent to the "flux in the solution phase" (indicated with $\mathbf{N}/\epsilon$ in Reference 43) and the "average flux in the pore solution" ($\mathbf{N}$ in Reference 43) that is "averaged over the cross-sectional area of the electrode,"[43] respectively. The integrals that refer to the positive electrode domain in (29) are equivalent to the weak forms of Equations (1), (2), (20), (23), and (24) of Newman and Tiedemann[43] for a binary electrolyte without convective motion. A crucial difference however exists with Reference 43: in the dimensionally reduced model the interaction between each jth fiber and the electrolyte is explicitly accounted for through the integrals over the fiber surface $S_{\text{int,am},j}$ (last term on the right-hand side of Equation 29), rather than considering a volume-averaged charge transfer ($a\, i_n$ in the reference). This feature is relevant to the modeling of battery electrodes in which the characteristic length of the active material inclusion is not negligible compared to the characteristic size of the electrode. Since active fibers can span a significant portion of the electrode thickness, the interaction between a single fiber and the response of the electrode as a whole does not reduce to an exchange term circumscribed to a single (electrode) macroscopic point.

The benefit of non-conformal meshes goes beyond the advantage brought by mortar-based approaches.[29] Even if they enable the use of non-conforming meshes for the discretization of active material inclusions and electrolyte, their geometries have to conform to one another, leading to very large system of equations for fiber volumes similar to those analyzed in this work. While mortar-based approaches can be applied to particles of any shape, our approach is ideal for large volumes of one-dimensional fibers.

The dimensionally reduced approach is tailored for fibrous electrode modeling, and approximation are introduced to promote its numerical efficiency. The numerical investigations described in Section 5 are performed to assess the simplifications introduced and the impact they have on the accuracy of the dimensionally reduced model. The verification is twofold. We check both the validity of the assumption of uniform fields on fiber cross section, and also the impact of the dimensional reduction of fibers on the global response of the system.

For numerical implementation purpose, weak forms (27)–(29) are recast into non-dimensional equivalent forms inspired by Salvadori et al.[44,45] This approach should eliminate convergence issues stemming from an ill-conditioned global tangent matrix. The interested reader can refer to Appendix A.1 in Reference 39 for an application of the non-dimensionalization to a set of governing equations similar to the one considered here.

4 | DISCRETIZATION AND FE APPROXIMATIONS

We describe the numerical implementation of the dimensionally reduced model tailored for fiber-shaped active material inclusions. The weak form of the governing equations is obtained through the substitution of constitutive equations provided in Table 3 and those of either Tables 1 or 2 into (23a), (24), (27), (28), and (29). The time-continuous system of equations is transformed into a corresponding incremental form by means of a backward-Euler integration scheme; nonlinearities are addressed by means of a classical incremental-iterative nonlinear solution procedure equipped with a Newton–Raphson iterative method.[46] In this section, we only provide details about the discretization of the positive electrode constituents as the discretization of the other cell components are treated using standard strategies.

4.1 | Spatial discretization at the element level

The electrolyte domain is discretized using isoparametric FE of the same dimensionality of the problem: eight-node hexahedral in a three-dimensional setting, and four-node quadrilateral elements in a two-dimensional setting. Fibers are discretized using one-dimensional isoparametric FEs irrespective of the dimensionality of the problem, and the same holds for fiber-electrolyte interfaces. In practice, integration over fiber volume and fiber surface only differ by a constant: area A_j and circumference C_j, respectively (cf. (25)/(23b) to (27)/(28)).

Active material inclusions and electrolyte

Electric potential and concentration fields at an arbitrary location in an electrolyte element are expressed as

$$\phi_{\text{el}} = \mathbf{N}_{\text{b}}\,\boldsymbol{\phi}_{\text{el}} \quad \text{and} \quad c_{\text{el}} = \mathbf{N}_{\text{b}}\,\boldsymbol{c}_{\text{el}}, \tag{30}$$

respectively, with bulk shape functions

$$\mathbf{N}_{\text{b}} = \begin{bmatrix} N_{\text{b1}} & \dots & N_{\text{b}n} \end{bmatrix}, \tag{31}$$

where n is the number of nodes in a bulk element and $N_{\text{b}i}$ is the ith nodal shape function. Vectors

$$\boldsymbol{\phi}_{\text{el}} = \begin{bmatrix} \phi_{\text{el1}} & \dots & \phi_{\text{el}n} \end{bmatrix}^{\text{T}} \quad \text{and} \quad \boldsymbol{c}_{\text{el}} = \begin{bmatrix} c_{\text{el1}} & \dots & c_{\text{el}n} \end{bmatrix}^{\text{T}} \tag{32}$$

collect nodal unknowns. Derivatives of bulk shape functions in the global coordinate system $\mathbf{x}$ are assembled in the discrete gradient operator

$$\mathbf{B}_{\text{b}} = \begin{bmatrix} \frac{\partial N_{\text{b1}}}{\partial x} & \dots & \frac{\partial N_{\text{b}n}}{\partial x} \\ \frac{\partial N_{\text{b1}}}{\partial y} & \dots & \frac{\partial N_{\text{b}n}}{\partial y} \\ \frac{\partial N_{\text{b1}}}{\partial z} & \dots & \frac{\partial N_{\text{b}n}}{\partial z} \end{bmatrix}. \tag{33}$$

The distribution of field variables along the axis of the fiber is described through a local scalar coordinate s (Figure 1). Electric potential and concentration fields at location s in a fiber element are thus expressed as

$$\phi_{\text{am}} = \mathbf{N}_{\text{f}}\,\boldsymbol{\phi}_{\text{am}} \quad \text{and} \quad c_{\text{am}} = \mathbf{N}_{\text{f}}\,\boldsymbol{c}_{\text{am}}, \tag{34}$$

respectively, with one-dimensional fiber shape functions

$$\mathbf{N}_{\text{f}} = \begin{bmatrix} N_{\text{f1}} & \dots & N_{\text{f}m} \end{bmatrix} \tag{35}$$

and vectors of nodal unknowns

$$\boldsymbol{\phi}_{\text{am}} = \begin{bmatrix} \phi_{\text{am1}} & \dots & \phi_{\text{am}m} \end{bmatrix}^{\text{T}} \quad \text{and} \quad \boldsymbol{c}_{\text{am}} = \begin{bmatrix} c_{\text{am1}} & \dots & c_{\text{am}m} \end{bmatrix}^{\text{T}} \tag{36}$$

for fiber elements with m nodes. The derivatives of the fiber shape functions are assembled in the discrete gradient operator

$$\mathbf{B}_{\text{f}} = \begin{bmatrix} \frac{\partial N_{\text{f1}}}{\partial s} & \dots & \frac{\partial N_{\text{f}m}}{\partial s} \end{bmatrix}, \tag{37}$$

here expressed in the local coordinate system. In this work, we use linear elements only ($m = 2$).

Active material-electrolyte interface

Weak form (28) is used to evaluate the current exchanged across the fiber-electrolyte interface. By introducing degree of freedom $i_{\text{BV,am}j}$ for each fiber element node and collecting the corresponding nodal values in the vector

$$\boldsymbol{i}_{\text{BV,am}} = \begin{bmatrix} i_{\text{BV,am1}} & \dots & i_{\text{BV,am}m} \end{bmatrix}^{\text{T}}, \tag{38}$$

the charge transfer can be approximated through

$$i_{\text{BV,am}} = \mathbf{N}_{\text{f}}\,\boldsymbol{i}_{\text{BV,am}} \tag{39}$$

at an arbitrary location along the fiber element. Shape functions $\mathbf{N}_f$ (35) are identical to those used to approximate the distribution of c_{am} and ϕ_{am} in the fiber element.

The computation of integral (28) requires the evaluation of $f_{BV,am}$ at the integration points of the one-dimensional fiber element (gray cross in Figure 1C.1). The procedure is described next and requires knowledge about fiber nodes and nodal degrees of freedom, all expressed in the global coordinate system. For each fiber element (i.e., either one of the three segments a, b, and c in Figure 1C.1) quantities $\boldsymbol{\phi}_{el}$ and $\boldsymbol{c}_{el}$ at the electrolyte element nodes are interpolated to quantities $\boldsymbol{\phi}_{f,el}$ and $\boldsymbol{c}_{f,el}$ at the fiber nodes through

$$\boldsymbol{\phi}_{f,el} = \mathbf{H}_f \, \boldsymbol{\phi}_{h,el} \quad \text{and} \quad \boldsymbol{c}_{f,el} = \mathbf{H}_f \, \boldsymbol{c}_{h,el}, \tag{40}$$

where, for a two-node fiber element,

$$\mathbf{H}_f = \begin{bmatrix} \mathbf{N}_b^A \big|_{\mathbf{x}_1} & \mathbf{0} \\ \mathbf{0} & \mathbf{N}_b^B \big|_{\mathbf{x}_2} \end{bmatrix}$$

is a $2 \times 2n$ array that gathers bulk shape functions of electrolyte elements A and B hosting fiber element nodes 1 and 2, respectively (for the sake of example, refer to fiber element b in Figure 1C.1). Array $\mathbf{H}_f$ is constructed by identifying the elements that contain the fiber nodes and evaluating the corresponding shape functions at that location. Since shape functions are defined in the element natural coordinate system, an inverse mapping is needed to express the coordinate of a fiber node, given in the global coordinate system, in the element domain. In the case of a fiber node on an element edge, it would be enough to select just one of the elements sharing that edge. The previous expression can be generalized to the case of a fiber element with m nodes; in that case, the array size is $m \times mn$. Vectors

$$\boldsymbol{\phi}_{h,el} = \begin{bmatrix} \boldsymbol{\phi}_{el}^A \\ \boldsymbol{\phi}_{el}^B \end{bmatrix} \quad \text{and} \quad \boldsymbol{c}_{h,el} = \begin{bmatrix} \boldsymbol{c}_{el}^A \\ \boldsymbol{c}_{el}^B \end{bmatrix}$$

collect nodal unknowns of electrolyte element A and B, respectively. The expression above is valid also when both nodes of the fiber element fall within the same electrolyte element, that is, when $\boldsymbol{\phi}_{el}^B = \boldsymbol{\phi}_{el}^A$ and $\boldsymbol{c}_{el}^B = \boldsymbol{c}_{el}^A$.

Finally, electric potential ϕ_{el} and concentration c_{el} at location s along the fiber element are thus expressed as

$$\phi_{el}(s) = \mathbf{N}_f \, \boldsymbol{\phi}_{f,el} = \mathbf{N}_f \mathbf{H}_f \, \boldsymbol{\phi}_{h,el} \quad \text{and} \quad c_{el}(s) = \mathbf{N}_f \, \boldsymbol{c}_{f,el} = \mathbf{N}_f \mathbf{H}_f \, \boldsymbol{c}_{h,el}, \tag{41}$$

where $\mathbf{N}_f \mathbf{H}_f$ is a combination of electrolyte and fiber element shape functions that interpolate from the nodes of the electrolyte elements hosting a node of the fiber element to a location along the fiber element. The procedure just described is general and works for any discretization.

4.2 | Element level implementation

We aim to provide an example of the FE implementation of the dimensionally reduced model to highlight the details of the numerical coupling between bulk electrolyte elements and dimensionally reduced fiber elements. For the sake of example, we consider the weak form of the governing equations obtained through the substitution of constitutive equations listed in Tables 1 and 3 into (23a), (24), (27), (28), and (29). When the constitutive equations of Table 2 are considered instead, the numerical implementation is analogous, just more laborious.

For simplicity, we assume that all fibers in the positive electrode have equal cross section, that is, $A_j = A$ and $C_j = C$ with $j = 1, \ldots, n_{am}$. We make use of symbol Ω_k^e with $k = am$ or el to indicate the integration over a single electrolyte or active fiber FE, respectively.

Active material sub-matrices

The contributions to the element residual vector and tangent matrix that follow from the space-time discretization of (27) read

$$
\mathbf{r}_{am}^{\phi} = \kappa_{am} \, A \, \int_{\Omega_{am}^e} \mathbf{B}_f^T \, \mathbf{B}_f \, \boldsymbol{\phi}_{am} \; d\Omega,
$$

$$
\mathbf{r}_{am}^{c} = \frac{A}{\Delta t} \int_{\Omega_{am}^e} \mathbf{N}_f^T \, \mathbf{N}_f \, \Delta \boldsymbol{c}_{am} \; d\Omega + D_{am} \, A \, \int_{\Omega_{am}^e} \mathbf{B}_f^T \, \mathbf{B}_f \, \boldsymbol{c}_{am} \; d\Omega, \tag{42}
$$

and

$$
\mathbf{K}_{am}^{\phi\phi} = \frac{\partial \mathbf{r}_{am}^{\phi}}{\partial \boldsymbol{\phi}_{am}} = \kappa_{am} \, A \, \int_{\Omega_{am}^e} \mathbf{B}_f^T \, \mathbf{B}_f \; d\Omega,
$$

$$
\mathbf{K}_{am}^{cc} = \frac{\partial \mathbf{r}_{am}^{c}}{\partial \boldsymbol{c}_{am}} = \frac{A}{\Delta t} \int_{\Omega_{am}^e} \mathbf{N}_f^T \, \mathbf{N}_f \; d\Omega + D_{am} \, A \, \int_{\Omega_{am}^e} \mathbf{B}_f^T \, \mathbf{B}_f \; d\Omega, \tag{43}
$$

respectively. Vectors $\boldsymbol{\phi}_{am}$ and $\boldsymbol{c}_{am}$ refer to the electric potential and concentration of the active material at current time increment and previous iteration. The concentration increment $\Delta \boldsymbol{c}_{am}$ is defined as the difference between the most updated (current time increment, previous iteration) and the last converged (previous time increment) solutions for the concentration in (36). The quantity Δt defines the time increment size.

Electrolyte sub-matrices

The contributions to the element residual vector and tangent matrix that follow from the space-time discretization (29) read

$$
\mathbf{r}_{el}^{\phi} = \gamma_{\phi} \, \epsilon \, \int_{\Omega_{el}^e} \mathbf{B}_b^T \, \mathbf{B}_b \, \boldsymbol{\phi}_{el} \, \mathbf{N}_b \, \boldsymbol{c}_{el} \; d\Omega \; - \; \gamma_c \, \epsilon \int_{\Omega_{el}^e} \mathbf{B}_b^T \, \mathbf{B}_b \, \boldsymbol{c}_{el} \; d\Omega,
$$

$$
\mathbf{r}_{el}^{c} = \frac{\epsilon}{\Delta t} \int_{\Omega_{el}^e} \mathbf{N}_b^T \, \mathbf{N}_b \, \Delta \boldsymbol{c}_{el} \; d\Omega + D_{el} \, \epsilon \int_{\Omega_{el}^e} \mathbf{B}_b^T \, \mathbf{B}_b \, \boldsymbol{c}_{el} \; d\Omega, \tag{44}
$$

and

$$
\mathbf{K}_{el}^{\phi\phi} = \frac{\partial \mathbf{r}_{el}^{\phi}}{\partial \boldsymbol{\phi}_{el}} = \gamma_{\phi} \, \epsilon \, \int_{\Omega_{el}^e} \mathbf{B}_b^T \, \mathbf{B}_b \, \mathbf{N}_b \, \boldsymbol{c}_{el} \; d\Omega,
$$

$$
\mathbf{K}_{el}^{\phi c} = \frac{\partial \mathbf{r}_{el}^{\phi}}{\partial \boldsymbol{c}_{el}} = \gamma_{\phi} \, \epsilon \, \int_{\Omega_{el}^e} \mathbf{B}_b^T \, \mathbf{B}_b \, \boldsymbol{\phi}_{el} \, \mathbf{N}_b \; d\Omega \; - \; \gamma_c \, \epsilon \int_{\Omega_{el}^e} \mathbf{B}_b^T \, \mathbf{B}_b \; d\Omega, \tag{45}
$$

$$
\mathbf{K}_{el}^{cc} = \frac{\partial \mathbf{r}_{el}^{c}}{\partial \boldsymbol{c}_{el}} = \frac{\epsilon}{\Delta t} \int_{\Omega_{el}^e} \mathbf{N}_b^T \, \mathbf{N}_b \; d\Omega + D_{el} \, \epsilon \int_{\Omega_{el}^e} \mathbf{B}_b^T \, \mathbf{B}_b \; d\Omega,
$$

respectively. Vectors $\boldsymbol{\phi}_{el}$ and $\boldsymbol{c}_{el}$ refer to the electrolyte electric potential and concentration vectors at current time increment and previous iteration.

Interface sub-matrices

The residual vectors corresponding to the last term in each of the equations in weak form (27) read

$$
\mathbf{r}_{am}^{\phi i} = C \int_{\Omega_{am}^e} \mathbf{N}_f^T \, \mathbf{N}_f \, \boldsymbol{i}_{BV,am} \; d\Omega, \qquad \mathbf{r}_{am}^{ci} = \frac{C}{F} \int_{\Omega_{am}^e} \mathbf{N}_f^T \, \mathbf{N}_f \, \boldsymbol{i}_{BV,am} \; d\Omega \; . \tag{46}
$$

In this section, for convenience, superscript i indicates quantities that refer to the charge transfer degrees of freedom $\boldsymbol{i}_{BV,am}$ (superscript i is, therefore, not to be understood as an index). The last term in each of the equations in weak form (29) is computed analogously, however, integrals must be evaluated for each electrolyte element that contains node of the fiber element on which integration is performed, that is,

$$
\mathbf{r}_{el}^{\phi i} = - \, C \int_{\Omega_{am}^e} \mathbf{N}_b^T \, \mathbf{N}_f \, \boldsymbol{i}_{BV,am} \; d\Omega, \qquad \mathbf{r}_{el}^{ci} = - \frac{C}{F} \frac{D_{X^-}}{D_{Li^+} + D_{X^-}} \int_{\Omega_{am}^e} \mathbf{N}_b^T \, \mathbf{N}_f \, \boldsymbol{i}_{BV,am} \; d\Omega, \tag{47}
$$

according to (40). According to (34) and (41), the discretization of weak form (28) leads to

$$
\mathbf{r}_{int}^{i} = C \int_{\Omega_{am}^e} \mathbf{N}_f^T \, \mathbf{N}_f \, \boldsymbol{i}_{BV,am} \; d\Omega - C \int_{\Omega_{am}^e} \mathbf{N}_f^T \, f_{BV,am} \left(\mathbf{N}_f \, \boldsymbol{\phi}_{am}, \; \mathbf{N}_f \mathbf{H}_f \, \boldsymbol{\phi}_{h,el}, \; \mathbf{N}_f \, \boldsymbol{c}_{am}, \; \mathbf{N}_f \mathbf{H}_f \, \boldsymbol{c}_{h,el} \right) \; d\Omega. \tag{48}
$$

Arrays $\mathbf{H}_f$ are assembled once and for all during preprocessing. The determination of the electrolyte element in which the fiber element nodes are located can be efficiently pursued by exploiting quadtree and octree data structures at the pre-processing stage for the structured eight-node hexahedral (Sections 5.1 and 5.2) and four-node quadrilateral (Section 5.3) FEs used to discretize the electrolyte domain, respectively.

The dimensionally reduced model entails a certain level of approximation. The accuracy of the numerical evaluation of quantities that depend on local field variables is subordinate to the validity of the assumption of uniform fields on fiber cross-sections (Section 3). The most direct consequence is on the numerical evaluation of the charge transfer through (48) (that particularizes according to either (8) or (13)) that is evaluated from nodal quantities $\boldsymbol{\phi}_{am}$ and $\boldsymbol{c}_{am}$ (36) of the one-dimensional representation of the fiber (no distinction between surface and bulk values applies to the dimensionally reduced model, Section 3) and nodal values of the bulk electrolyte elements interpolated at the fiber nodes $\boldsymbol{\phi}_{f,el}$ and $\boldsymbol{\phi}_{f,el}$ (40). Due to this simplified treatment, the evolution of $i_{0,am}$, η_{am}, and $i_{BV,am}$ during the discharge process is, in general, different compared to a fully resolved model. The quantification of the discrepancies between responses obtained with fully resolved and dimensionally reduced models as well as the identification of the causes of the discrepancies are addressed in Section 5.1.

The contribution of the interface terms to the tangent matrix are evaluated as follows

$$
\begin{aligned}
&\mathbf{C}_{am}^{\phi i} = \frac{\partial \mathbf{r}_{am}^{\phi i}}{\partial \boldsymbol{i}_{BV,am}} = C \int_{\Omega_{am}^e} \mathbf{N}_f^T \, \mathbf{N}_f \; d\Omega, &&\mathbf{C}_{am}^{ci} = \frac{\partial \mathbf{r}_{am}^{ci}}{\partial \boldsymbol{i}_{BV,am}} = \frac{C}{F} \int_{\Omega_{am}^e} \mathbf{N}_f^T \, \mathbf{N}_f \; d\Omega, \\[2mm]
&\mathbf{C}_{el}^{\phi i} = \frac{\partial \mathbf{r}_{el}^{\phi i}}{\partial \boldsymbol{i}_{BV,am}} = -C \int_{\Omega_{am}^e} \mathbf{N}_b^T \, \mathbf{N}_f \, \boldsymbol{i}_{BV,am} \; d\Omega, &&\mathbf{C}_{el}^{ci} = \frac{\partial \mathbf{r}_{el}^{ci}}{\partial \boldsymbol{i}_{BV,am}} = -\frac{C}{F} \frac{D_{X^-}}{D_{Li^+} + D_{X^-}} \int_{\Omega_{am}^e} \mathbf{N}_b^T \, \mathbf{N}_f \, \boldsymbol{i}_{BV,am} \; d\Omega, \\[2mm]
&\mathbf{C}_{int}^{i\phi_{am}} = \frac{\partial \mathbf{r}_{int}^i}{\partial \boldsymbol{\phi}_{am}} = -C \int_{\Omega_{am}^e} \mathbf{N}_f^T \, \frac{\partial f_{BV,am}}{\partial \boldsymbol{\phi}_{am}} \; d\Omega, &&\mathbf{C}_{int}^{ic_{am}} = \frac{\partial \mathbf{r}_{int}^i}{\partial \boldsymbol{c}_{am}} = -C \int_{\Omega_{am}^e} \mathbf{N}_f^T \, \frac{\partial f_{BV,am}}{\partial \boldsymbol{c}_{am}} \; d\Omega, &&(49)\\[2mm]
&\mathbf{C}_{int}^{i\phi_{el}} = \frac{\partial \mathbf{r}_{int}^i}{\partial \boldsymbol{\phi}_{el}} = -C \int_{\Omega_{am}^e} \mathbf{N}_f^T \, \frac{\partial f_{BV,am}}{\partial \boldsymbol{\phi}_{el}} \; d\Omega, &&\mathbf{C}_{int}^{ic_{el}} = \frac{\partial \mathbf{r}_{int}^i}{\partial \boldsymbol{c}_{el}} = -C \int_{\Omega_{am}^e} \mathbf{N}_f^T \, \frac{\partial f_{BV,am}}{\partial \boldsymbol{c}_{el}} \; d\Omega, \\[2mm]
&\mathbf{C}_{int}^{ii} = \frac{\partial \mathbf{r}_{int}^i}{\partial \boldsymbol{i}_{BV,am}} = C \int_{\Omega_{am}^e} \mathbf{N}_f^T \, \mathbf{N}_f \; d\Omega.
\end{aligned}
$$

Vectors $\boldsymbol{\phi}_{am}$, $\boldsymbol{c}_{am}$, $\boldsymbol{\phi}_{el}$, and $\boldsymbol{c}_{el}$, used to compute $f_{BV,am}$ and its derivatives, and vector $\boldsymbol{i}_{BV,am}$ are evaluated at current time increment and previous iteration.

4.3 | Global system of equations

The vector of all nodal unknowns is defined as

$$
\mathbf{u} = \begin{bmatrix} \overline{\boldsymbol{\phi}}_{el}^{\;T} & \overline{\boldsymbol{\phi}}_{am}^{\;T} & \overline{\boldsymbol{c}}_{el}^{\;T} & \overline{\boldsymbol{c}}_{am}^{\;T} & \overline{\boldsymbol{i}}_{BV,am}^{\;T} \end{bmatrix}^T,
$$

where vectors $\overline{\boldsymbol{\phi}}_{el}$, $\overline{\boldsymbol{\phi}}_{am}$, $\overline{\boldsymbol{c}}_{el}$, $\overline{\boldsymbol{c}}_{am}$, and $\overline{\boldsymbol{i}}_{BV,am}$ collect nodal unknowns (32), (36), and (38) of all elements. At each time step and for each kth iteration of the Newton–Raphson iterative scheme we seek for the increment $\delta \mathbf{u}^k$ such that

$$
\mathbf{u}^k = \mathbf{u}^{k-1} + \delta \mathbf{u}^k
$$

solving the linear system of equations

$$
\overline{\mathbf{K}} \, \delta \mathbf{u}^k = -\overline{\mathbf{r}}^{\,k-1},
$$

where the residual vector

$$
\overline{\mathbf{r}}^{\,k-1} \equiv \mathbf{f}^{int}\left(\mathbf{u}^{k-1} \right) - \mathbf{f}^{ext}, \tag{50}
$$

and

$$\delta \mathbf{u} = \begin{bmatrix} \delta \overline{\boldsymbol{\phi}}_{am} \\ \delta \overline{\boldsymbol{c}}_{am} \\ \delta \overline{\boldsymbol{\phi}}_{el} \\ \delta \overline{\boldsymbol{c}}_{el} \\ \delta \overline{\boldsymbol{i}}_{BV,am} \end{bmatrix}, \qquad \mathbf{f}^{int} = \begin{bmatrix} \overline{\mathbf{r}}^{\phi}_{am} + \overline{\mathbf{r}}^{\phi i}_{am} \\ \overline{\mathbf{r}}^{c}_{am} + \overline{\mathbf{r}}^{ci}_{am} \\ \overline{\mathbf{r}}^{\phi}_{el} + \overline{\mathbf{r}}^{\phi i}_{el} \\ \overline{\mathbf{r}}^{c}_{el} + \overline{\mathbf{r}}^{ci}_{el} \\ \overline{\mathbf{r}}^{i}_{int} \end{bmatrix}, \qquad \text{and} \qquad \overline{\mathbf{K}} = \begin{bmatrix} \overline{\mathbf{K}}^{\phi\phi}_{am} & 0 & 0 & 0 & \overline{\mathbf{C}}^{\phi i}_{am} \\ 0 & \overline{\mathbf{K}}^{cc}_{am} & 0 & 0 & \mathbf{C}^{ci}_{am} \\ 0 & 0 & \overline{\mathbf{K}}^{\phi\phi}_{el} & \overline{\mathbf{K}}^{\phi c}_{el} & \overline{\mathbf{C}}^{\phi i}_{el} \\ 0 & 0 & 0 & \overline{\mathbf{K}}^{cc}_{el} & \overline{\mathbf{C}}^{ci}_{el} \\ \overline{\mathbf{C}}^{i\phi_{am}}_{int} & \overline{\mathbf{C}}^{ic_{am}}_{int} & \overline{\mathbf{C}}^{i\phi_{el}}_{int} & \overline{\mathbf{C}}^{ic_{el}}_{int} & \overline{\mathbf{C}}^{ii}_{int} \end{bmatrix}. \qquad (51)$$

Submatrices $\overline{\mathbf{K}}^{lj}_{am/el}$ collect the contributions of the corresponding element tangent matrices (43) and (45) assembled over the active material and electrolyte domains, and submatrices $\overline{\mathbf{C}}^{lj}_{am/el/int}$ gather the element contributions of the interface terms (49). Subvectors $\overline{\mathbf{r}}^{l}_{am/el/int}$ collect the contributions of the corresponding element residual vectors (42), (44), and (48), assembled over the active material and electrolyte domains, and interfaces. Subvectors $\overline{\mathbf{r}}^{lj}_{am/el}$ collect the contributions of the element residual vectors (46) and (47), assembled over the interfaces. We remark that, in the actual linear system of equations, the so-called "internal global force" vector $\mathbf{f}^{int46}$ and matrix $\overline{\mathbf{K}}$ must include also the terms that descend from the discretization of the negative electrode. Vector $\overline{\mathbf{r}}^{k-1}$ includes the boundary conditions through the so-called "external global force" vector $\mathbf{f}^{ext}$,[46] whose definition is standard argument in FE. The representation in (51) emphasizes the relationship established between nodal quantities that belong to different domains through $\overline{\boldsymbol{i}}_{BV,am}$.

As shown by Goudarzi et al.,[47] an advantage of the embedded approach over classical conformal FEM discretization is the possibility of efficiently condensing out all the degrees of freedom related to fiber segments. The procedure yields a global system of equations with the same size as that of the matrix without fibers.

5 | NUMERICAL EXAMPLES

The capability of the dimensionally reduced model to simulate electrochemical processes in fibrous battery electrodes is assessed by comparing simulation results against reference solutions from the literature and results obtained with the fully resolved model. An analysis of the cell voltage response and the evolution of the local fields (c_{am}, c_{el}, and i_{BV}) is part of the evaluation.

In Section 5.1, we consider a single-fiber positive electrode in a three-dimensional setting. The impact of the fiber geometrical features and discharge rate on the response of the dimensionally reduced model is evaluated using the fully resolved model results as a reference solution. The dimensionally reduced model is tested in Section 5.2 on a positive electrode with roughly 25,000 active fibers in a three-dimensional setting. To the best of the authors' knowledge, this is the first work to present a numerical tool for the modeling and simulation of arbitrary distributions of discrete fibers in a fibrous battery electrode. Since no reference solution is available for fibrous battery electrodes and the solution of the fully resolved model is not currently achievable for such a geometry, we select the pseudo-2D model results by Doyle et al.[21] as reference solution. A similar approach has been followed in the literature, with the pseudo-2D model providing reference solutions for more sophisticated models (e.g., References 13, 14, and 48). Finally, Section 5.3 examines the evolution of the charge transfer on the fiber-electrolyte interface by comparing results obtained with dimensionally reduced and fully resolved models for a two-fiber positive electrode in a two-dimensional setting.

The numerical examples are performed using the same cell components and material parameters as Doyle et al.[21] Figure 1A shows the domains forming the cell: (i) homogeneous lithium foil as the negative electrode; (ii) separator layer of polyethylene oxide-lithium trifluoromethane sulfonate (PEO-LiCF$_3$SO$_3$); (iii) positive electrode made of titanium disulfide (TiS$_2$) active material inclusions embedded in PEO-LiCF$_3$SO$_3$. Quantities that are repeatedly referred to in the discussion of the numerical example are defined next.

State of charge

We express the state of charge (SOC) of the positive electrode as

$$\text{SOC} = \frac{c_{am,avg}}{c_{am}^{max}}, \qquad (52)$$

where $c_{am,avg}$ is the average concentration of lithium in the active material of the positive electrode, and c_{am}^{max} is the saturation limit of lithium in the active material. For a galvanostatic process, the relation

$$c_{am,avg} = \frac{I\,t}{F\,(1-\epsilon)\,\delta_{pos}} + c_{am}^0$$

holds, where I is the current applied according to boundary condition (19a), δ_{pos} is the thickness of the positive electrode, c_{am}^0 is the initial concentration of the lithium in the active material, and t is the time elapsed since the beginning of the process.

Cell potential

The cell potential

$$\Delta\phi = \phi_{am} - \phi_{neg}(x = -\delta_{neg})$$

simplifies into

$$\Delta\phi = -\phi_{neg}(x = -\delta_{neg}) \tag{53}$$

TABLE 4 Material parameters and initial condition values common to all numerical examples

Domain	Quantity	Symbol	Value	Equation
V_{neg} (lithium foil)	Li diffusivity[a]	D_{neg}	1.0×10^{-11} m^2 s^{-1}	
	Electronic conductivity[a]	κ_{neg}	1.0×10^6 S m^{-1}	
	Initial concentration Li[b]	c_{neg}^0	85,000 mol m^{-3}	
V_{el} (PEO-LiCF$_3$SO$_3$)	Initial concentration LiCF$_3$SO$_3$	c_{el}^0	1000 mol m^{-3}	
	Saturation limit LiCF$_3$SO$_3$	c_{el}^{max}	3920 mol m^{-3}	
V_{am} (TiS$_2$)	Li diffusivity	D_{am}	5.0×10^{-13} m^2 s^{-1}	
	Initial concentration Li	c_{am}^0	100 mol m^{-3}	
	Saturation limit Li	c_{am}^{max}	29,000 mol m^{-3}	
$S_{int,neg}$	Exchange current density[c]	$i_{0,neg} = F\,k_{neg}\left(c_{el}^{max} - c_{el}\right)^{\alpha_c} c_{el}^{\alpha_a}$		(54)
	Open circuit potential	$U_{OC,neg}$	0	(55)
	Reaction rate constant	k_{neg}	7.6422×10^{-8} m s^{-1}	
$S_{int,am}$	Exchange current density[c]	$i_{0,am} = F\,k_{am}\left(c_{el}^{max} - c_{el}\right)^{\alpha_c} c_{el}^{\alpha_a} \left(c_{am}^{max} - c_{am}\right)^{\alpha_a} c_{am}^{\alpha_c}$		(56)
	Open circuit potential[c]	$U_{OC,am} = U_{ref} + \frac{RT}{F}\left(\ln\left(\frac{c_{am}^{max}-c_{am}}{c_{am}}\right) + \beta c_{am} + \zeta\right)$		(57)
	Reaction rate constant	k_{am}	10^{-10} m^4 mol^{-1} s^{-1}	
	Reference open potential	U_{ref}	2.17 V	
	First coefficient	β	-0.000558 m^3 mol^{-1}	
	Second coefficient	ζ	8.10	
Entire cell	Faraday's constant	F	96,485.3 C mol^{-1}	
	Ideal gas constant	R	8.31447 J K^{-1} mol^{-1}	
	Temperature	T	373.15 K	
	Apparent transfer coefficients	α_a, α_c	0.5	

Note: All the data are from Doyle et al.[21] unless otherwise specified.

[a]Lithium diffusivity and electronic conductivity are chosen assuming that the negative electrode is an ideal reservoir of lithium and a perfect conductor.

[b]Value computed considering a theoretical specific capacity of 3860 mA h g^{-1} and a density of 0.59 g cm^{-3}.[49]

[c]Concentration expressed in mol m^{-3}.

TABLE 5 Material parameters suitable for the electrolyte constitutive model described in Table 1

Property	Symbol	Value	Units
Li$^+$ diffusivity[a]	D_{Li^+}	4.46×10^{-12}	m^2 s^{-1}
CF$_3$SOSO$_3^-$ diffusivity[a]	D_{X^-}	23.4×10^{-12}	m^2 s^{-1}

[a]Values determined inverting expressions $D_{ionic} = 2D_{Li^+} D_{X^-} / (D_{Li^+} + D_{X^-})$, and $t_+^0 = D_{Li^+} (D_{Li^+} + D_{X^-})$,[37] where $D_{ionic} = 7.5 \times 10^{-12}$ m^2 s^{-1} and $t_+^0 = 0.160$ are the electrolyte diffusion coefficient and transference number provided in Reference 21 for $c_{el} = c_{el}^0$, respectively. We assume constant values of D_{Li^+} and D_{X^-} and employ the same values in separator and positive electrode.

because of (20). Since we assume that the negative electrode is a perfect conductor, the electric potential ϕ_{neg} is uniform on the cross-section (yz-plane) at $x = -\delta_{neg}$ (Figure 1). The numerical simulations are interrupted when the cell potential falls below the cutoff voltage, which is set to 1.7 V according to Doyle et al.[21]

5.1 | Dimensionally reduced versus fully resolved model: Single fiber investigation

We assess the capability of the dimensionally reduced model to approximate the response of the fully resolved model through a numerical example that allows a direct comparison between the two approaches. The same governing equations are used for the two models: they are obtained using the constitutive relations listed in Tables 1 and 3 into balance equations (1) for each domain V_{neg}, V_{el}, and V_{am}. The material parameters are listed in Tables 4 and 5. The formulation of Table 1 is preferred for this investigation because it is characterized by weaker nonlinearities and a smaller number of parameters compared to the formulation of Table 2. This allows us to focus on the key aspects of the active fiber-electrolyte interaction.

In the remainder of this section, we refer to

$$\Delta\theta_{rel} = \frac{\theta_{DR} - \theta_{FR}}{\theta_{FR}} \times 100 \tag{58}$$

as the relative difference between the values of quantity θ obtained with the dimensionally reduced (DR) and fully resolved (FR) models.

Figure 1 (panels (A) and (D)) shows a two-dimensional schematic of the three-dimensional geometry used in the numerical simulations. The cell consists of a lithium plate (negative electrode) and a fiber (positive) electrode of thickness $\delta_{neg} = 10$ μm and $\delta_{pos} = 80$ μm, respectively. The latter is comprised of a single active material fiber of length $l_f = 60$ μm and the surrounding electrolyte. The axis of the fiber is perpendicular to the lithium plate, and the fiber left end is located at $x = \delta_s = 20$ μm. The battery cell has a uniform out-of-plane cross-section with measure $A_s = L^2$, with $L = 100$ μm, and the axis of the fiber is placed at its center. Simulations are performed with fiber diameters d_f such that $d_f/L = 0.01, 0.05, 0.1, 0.2$, and 0.4, with aspect ratio l_f/d_f of the fiber equal to 60, 12, 6, 3, 1.5, respectively. The geometry with $l_f/d_f = 1.5$ by no means represents a slender object, but it is selected as the upper bound while investigating the range of applicability of the dimensionally reduced approach. The positive electrode porosity needed for the dimensionally reduced model simulations (refer to Section 3) is calculated as $\epsilon = 1 - V_{am}/\delta_{pos}^3$, where V_{am} equals the volume V_f of the fiber.

In the fully resolved model simulations, we use a non-structured discretization of four-node tetrahedral elements. The number of nodes of the discretization increases from about 2500 to about 11,000 as d_f/L reduces from 0.4 to 0.01 (since fiber and electrolyte meshes are conforming at the interface, the element sizes in the fiber and surrounding electrolyte are equally reduced). In the dimensionally reduced model simulations, lithium plate and electrolyte are discretized using a structured mesh of $4 \times 15 \times 15$ and $15 \times 15 \times 15$ eight-node hexahedral elements, respectively, and the fiber is discretized using 50 equally sized line elements. The number of discretization nodes amounts to about 5400 irrespective of the fiber diameter. The grid is fine enough to adequately capture gradients in the solution fields for the smallest value of the diameter (and too fine for the largest ones where coarser grids could have been used). Such a discretization setting has been chosen to show that parametric studies in terms of fiber geometrical quantities (the diameter in this case) can be addressed with just one fixed discretization in the reduced model.

We apply boundary and initial conditions described in Sections 2.4 and 2.5, respectively. In addition, we impose the mass flux and electric current density to be null across (i) the external surfaces of the simulation domain parallel to the

axis of the fiber and (ii) the external surface at $x = \delta_s + \delta_{pos}$. We perform simulations at 1 C rate discharge by applying the current density

$$I = \frac{c_{am}^{max} \, F \, V_{am}}{A_s \, t_d}, \tag{59}$$

where $c_{am}^{max} \, F \, V_{am}$ represents the capacity of the positive electrode, and t_d is the discharge time set equal to 1 h. Simulations have been performed with a constant time increment $\Delta t = 5$ s unless otherwise specified.

During discharge, the lithium insertion process stops either when the lithium concentration reaches the saturation limit on the surface of the fiber or when the surrounding electrolyte is depleted of lithium, as dictated by the exchange current density definition (56). The lithium concentration profile on a fiber cross-section is, in general, nonuniform. Due to the symmetry of the problem, the concentration on an arbitrary fiber cross-section far from the two circular edges is maximum at the fiber-electrolyte interface (where lithium insertion takes place) and is minimum at the center. Since (56) is evaluated assuming a uniform concentration over the fiber cross-section in the dimensionally reduced model, the responses of the fully resolved and dimensionally reduced models differ when a strong concentration gradient develops along the fiber radius. We aim to assess the capability of the dimensionally reduced model to describe: (i) the local evolution of the field variables, (ii) the conditions that cause the interruption of the charge transfer across the fiber-electrolyte interface, and (iii) the impact of these factors on the cell potential curve. We focus on the roles of fiber geometry and discharge rate. The numerical simulations described in this section are performed neglecting the dependence of the open circuit potential on the lithium content of the active material (57) (we set $U_{OC,am} = U_{ref}$).

We first assess the performance of the dimensionally reduced model through an examination of local fields such as concentration distribution within fiber and surrounding electrolyte, and fiber-electrolyte charge transfer across the interface. As a preliminary verification of the numerical implementation, we check (post-processing stage) that equality

$$I \, A_s \, t = F \int_{V_{am}} c_{am} - c_{am}^0 \, dV \tag{60}$$

holds at any time t of the numerical simulations. Satisfaction of equality (60) confirms that (i) the lithium content in the fiber is proportional to the charge transferred and (ii) lithium is neither artificially generated nor consumed. The right-hand side of (60) is evaluated through numerical integration over the elements representing the fiber, that is, one- and three-dimensional elements for dimensionally reduced model and fully resolved model, respectively.

Figure 2A shows the evolution of the lithium concentration distribution along the fiber length for a selection of fiber diameters ($d_f/L = 0.01, 0.05, 0.4$ with $l_f/d_f = 60, 12, 1.5$, respectively). For the fully resolved model, we report the values at the nodes located along the fiber axis. The concentration profiles obtained with dimensionally reduced and fully resolved models are consistent: the pointwise relative difference is 11% at the most (for $d_f/L = 0.4$, which is a very thick fiber with aspect ratio $l_f/d_f = 1.5$). In general, the smaller the fiber diameter the better the agreement between the results of the two models. The reason for this behavior is twofold. First, the magnitude of the concentration variation on the fiber cross-section is directly proportional to the fiber radius. Second, the influx of lithium from the circular edges (especially the one close to the lithium plate) is directly proportional to the surface, and thus to the radius. Since the dimensionally reduced model is insensitive to these aspects (Section 3), it better approximates the fully resolved model response as the fiber radius reduces.

Figure 2A shows that the curves of the concentration profile obtained with the dimensionally reduced model lie below those obtained with the fully resolved model for $d_f/L = 0.01$ and 0.05. The discrepancy is caused by the approximate representation of a cylindrical volume by means of four-node tetrahedral FEs: the about 18,000 FEs discretization (about 7400 for the fiber) used to obtain the results of Figure 2 with $d_f/L = 0.05$ leads to an underestimation of the actual fiber volume of about 3%, and thus causes an erroneous overestimation of the concentration. Two remarks support this conclusion. First, we observe that Equation (60) holds irrespective of the numerical approach if the integral is performed on the discretized domain (i.e., the actual fiber volume in the numerical simulation). Second, the extent of the mismatch is directly proportional to the amount of lithium in the fiber: because of (60), the lithium content in the fiber is the same in both models and therefore the concentration is on average higher in the fully resolved model because it underestimates the fiber volume. Since the evaluation of the fiber volume is intrinsically exact with the dimensionally reduced model (Section 3), the approach is especially convenient when the representation of a fiber with the fully resolved model requires an unreasonably fine mesh.
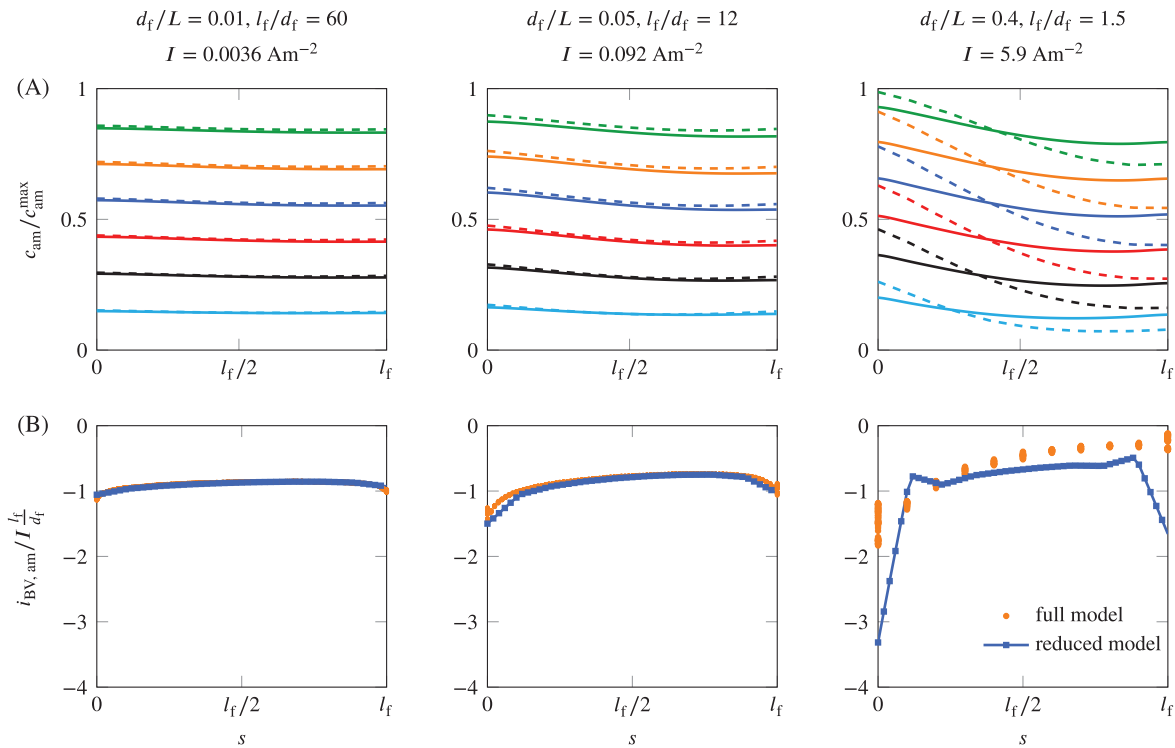
FIGURE 2 Effect of fiber diameter on local fields obtained with fully resolved and dimensionally reduced models for a cell with one fiber. (A) Concentration distribution along the length of the fiber at SOC = 0.14, 0.28, 0.42, 0.56, 0.69, and 0.83. Solid and dashed lines refer to reduced and fully resolved model, respectively. The fully resolved model results refer to the fiber axis. (B) Charge transfer along the length of the fiber for various fiber diameters at SOC = 0.5. The results of the fully resolved model (orange dots) are reported for all the nodes that belong to the fiber-electrolyte interface

An analysis of the results of the fully resolved model shows that the maximum difference between the concentration at the surface and at the center of the fiber cross section is modest. If we consider the concentration distribution in the fiber at SOC = 0.83 (i.e., when the difference between fully resolved and dimensionally reduced model is maximum in Figure 2A), the maximum difference is 0.04% with $l_f/d_f = 60$, 0.11% with $l_f/d_f = 12$, and 6.31% with $l_f/d_f = 1.5$ with respect to the average cross section concentration. With the set of parameters considered for the active material, it is reasonable to assume that the deviations of the local solution values on the fiber cross section from the cross-sectional average values are negligible for fibers with high aspect ratio (i.e., for $l_f/d_f \geq 12$).

Figure 2B shows the charge transfer distribution resulting from the two modeling approaches. The results are presented in terms of the distribution of charge transfer $i_{BV,am}$ (normalized by the product of applied current I and aspect ratio l_f/d_f) along the fiber length at SOC = 0.5 for the same fiber diameters considered in Figure 2A. The results of the fully resolved model are reported for the nodes at the fiber-electrolyte interface. We observe that the profiles of the dimensionally reduced model replicate those of the fully resolved model for slender fibers ($d_f/L \leq 0.1$, $l_f/d_f \geq 6$): for a fixed axial fiber coordinate, the maximum relative difference between the nodal value of the dimensionally reduced model and the average over the circular interface of the fully resolved model is about 15% (for $d_f/L = 0.1$). The weaker agreement found for the case of thick fibers (i.e., when $d_f/L \geq 0.2$, $l_f/d_f \leq 3$) can be explained as follows. First, concentration variations along the fiber radius are directly proportional to the fiber diameter. Second, the lithium influx across the two circular edges becomes substantial as the fiber aspect ratio reduces (as way of example, the contribution of the two circular edges is 25% of the whole fiber-electrolyte interface surface when $l_f/d_f = 1.5$). Even if fibers with larger diameters are subject to higher current densities (59), the contribution of the increased value of I to the mismatch between dimensionally reduced and fully resolved models is secondary compared to the two aspects just mentioned as demonstrated by the investigation described at the end of this section.

Figure 3 shows the concentration distribution in the electrolyte obtained with fully resolved (Figure 3A) and dimensionally reduced (Figure 3B) models for $d_f/L = 0.05$ ($l_f/d_f = 12$). The contour plots refer to SOC = 0.5 (the concentration distribution pattern for SOC = 0.5 is representative of most of the discharge process) for a simulation performed at
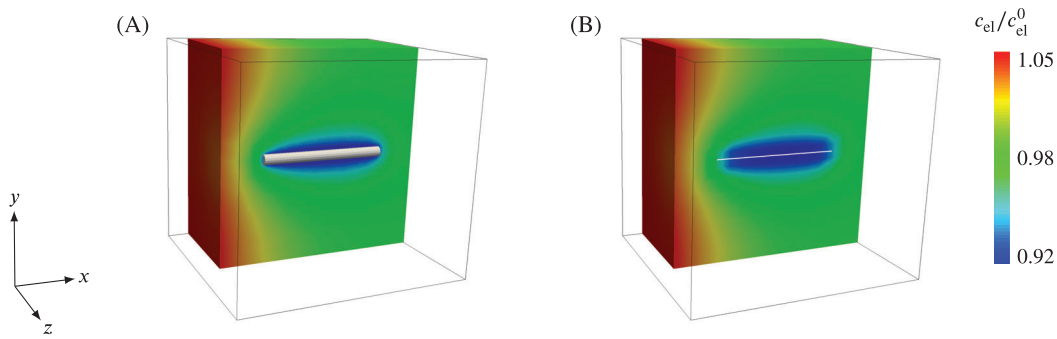
FIGURE 3 Visual comparison between results obtained with fully resolved (A) and dimensionally reduced (B) models for $d_f/L = 0.05$ ($l_f/d_f = 12$) in a cell with one fiber. Concentration distributions in the electrolyte during a 16 C rate discharge process ($I = 1.5$ A m^{-2}) at SOC = 0.5
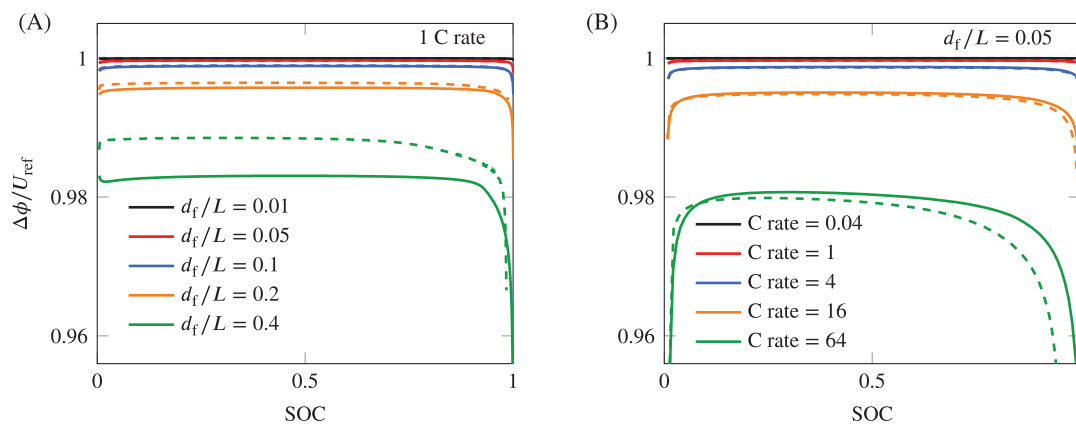

FIGURE 4 Comparison between results obtained with dimensionally reduced (solid lines) and fully resolved (dashed lines) models in terms of discharge curve: (A) influence of fiber diameter (d_f/L ranging from 0.01 to 0.4) for fixed discharge rate (1 C rate). (B) Influence of discharge rate (C rate ranging from 0.04 to 64, with current density ranging from $I = 3.6 \times 10^{-3}$ to 5.9 A m^{-2}) for a fiber with $d_f/L = 0.05$

16 C rate ($I = 1.5$ A m^{-2}). Both approaches yield visually similar results. This qualitative comparison further confirms the previous quantitative comparisons.

Next, we evaluate the performance of the reduced model in predicting the overall cell response through the analysis of discharge curves. Figure 4A shows the cell potential (53) as a function of the SOC (52) for all values of fiber diameter considered in the study. The trend of the curves is dictated by the dependence of the exchange current density on the concentration within the fiber (56). Indeed, Figure 3 shows that the concentration redistribution within the electrolyte is modest. The cell potential drops when the fiber concentration c_{am} approaches the saturation limit c_{am}^{max} on a large portion of the fiber surface because the exchange current density (56) approaches zero. The results of the dimensionally reduced and fully resolved models show the same trend: the maximum cell potential relative difference (58) is 3% at the most ($d_f/L = 0.4$, $l_f/d_f = 1.5$). Since the fiber surface concentration determined with the fully resolved model exceeds the average cross-sectional concentration determined with the dimensionally reduced model (for assigned instant of time and fiber cross-section), the exchange current density (56) and the cell potential (53) evaluated with the fully resolved model drop to zero at a slightly lower SOC.

The cell potential determined with the fully resolved model exceeds that of the dimensionally reduced model in all the numerical simulations performed at 1 C rate (Figure 4A). This is attributed to the twofold contribution of the circular edges to the lithium insertion process. First, since the distance between negative electrode and circular edge of the fiber is shorter than the distance between negative electrode and fiber body, the length of the lithium ion transport path reduces, and so does the resistivity of the system. Second, the different fiber-electrolyte interface surfaces of the two fiber representations (dimensionally reduced and fully resolved models) impact the average value of $i_{BV,am}$. The fiber surface available for charge

TABLE 6 Concentration-dependent material parameters suitable for the electrolyte constitutive model described in Table 2

Property	Symbol	Value/expression	Units
Electrolyte diffusivity[a]	D_{el}	7.5×10^{-12}	$m^2\,s^{-1}$
Electrolyte conductivity[a]	κ_{el}	$a_0 + a_1\,c_{el} + a_2\,c_{el}^2 + a_3\,c_{el}^3$ $a_0 = -5.0891863844 \times 10^{-3}$ $a_1 = 8.38645199394 \times 10^{-5}$ $a_2 = -5.19747901855 \times 10^{-8}$ $a_3 = 8.0832709407 \times 10^{-12}$	$S\,m^{-1}$
Transference number[b]	t_{el}	$0.0107907 + 1.48837 \times 10^{-4}\,c_{el}$	–
Mean molar activity coefficient variation[b]	$\frac{\partial \ln f_{el}}{\partial \ln c_{el}}$	0	–

Note: Concentration c_{el} should be expressed in $mol\,m^{-3}$.

[a]Values from References 50 and 51 for triflate in PEO.

[b]Values from Reference 21.

transfer exceeds that of the dimensionally reduced model and thus a lower overpotential is needed to transfer the same amount of charge.

Figure 4B shows the impact of the current density on the dimensionally reduced model response when a fiber with $d_f/L = 0.05$ ($l_f/d_f = 12$) is discharged at C rate ranging from 0.04 to 64. The values of the current density I (19a) are $I = 0.0036, 0.092, 0.37, 1.5,$ and $5.9\,A\,m^{-2}$, and they correspond to 1 C rate discharge for the five fiber diameters considered so far. In this set of simulations, Δt is adapted to each simulation to ensure that the increment of the SOC (for each time increment) is the same at all C rates. The reference is a time increment $\Delta t = 5\,s$ for a 1 C rate process. The results of the dimensionally reduced model replicate the trends of the results obtained with the fully resolved model irrespective of the value of the applied current. Differences between the results of the two models are detectable for $I = 5.9\,A\,m^{-2}$ (i.e., 64 C rate), which is a rather high value. For example, the results reported in Section 5.2 show that the average current density experienced by a single fiber with aspect ratio $l_f/d_f = 15$ is about $0.2\,A\,m^{-2}$ at the most when the fiber is part of a fibrous electrode subject to an overall $10\,A\,m^{-2}$ current density (corresponding to a 0.2 C rate discharge process).

5.2 | Porous electrode

In this section, we illustrate the capability of the dimensionally reduced model to simulate electrodes with multiple active fibers. The governing equations are obtained using the constitutive relations listed in Tables 2 and 3 into balance equations (1) for domains V_{neg}, V_{el}, and V_{am}. The material parameters are listed in Tables 4 and 6. The formulation is equivalent to the formulation by Doyle et al.,[21] whose results are used to validate our dimensionally reduced model. In the investigation performed by Doyle et al.,[21] the thicknesses of separator and positive electrode are $\delta_s = 50\,\mu m$ and $\delta_{pos} = 100\,\mu m$, respectively. Spherical active particles of diameter $d_p = 2\,\mu m$ occupy 70% of the positive electrode volume.

We consider the same cell geometry as Doyle et al.[21] but we replace the positive particle-electrode with a fibrous-electrode. We consider fibers with diameter $d_f = 2/3\,d_p = 1.3\,\mu m$ to ensure that the specific surfaces per unit volume of fibrous- and particle-electrodes are equal (being the fibers surface evaluated as $S_f = \pi d_f l_f$). We also chose a fiber length $l_f = 20\,\mu m$ to ensure that ratios $l_f/d_f = 15$ and $d_f/L = 0.013$ fall in the range where the dimensionally reduced model performance corresponds to the best compromise between accuracy and computational efficiency (Section 5.1). The thickness of the lithium plate and the size of the simulation domain in y and z directions are arbitrarily set equal to $\delta_{neg} = 30\,\mu m$ and $L = 100\,\mu m$, respectively. A two-dimensional schematic is depicted in Figure 1A, with the positive electrode reported in Figure 1E; Figure 5 shows the actual fiber distribution.

The active material volume fraction in the positive electrode is the same as Doyle et al.[21] ($\epsilon = 0.3$). The positive electrode geometry is generated using the random sequential adsorption technique[52] by selecting fiber coordinates and orientation angles from a uniform distribution and allowing fibers to overlap. The resulting fiber distribution is homogeneous, with no apparent preferential orientation: the uniform porosity assumption in Section 3 is thus met. This
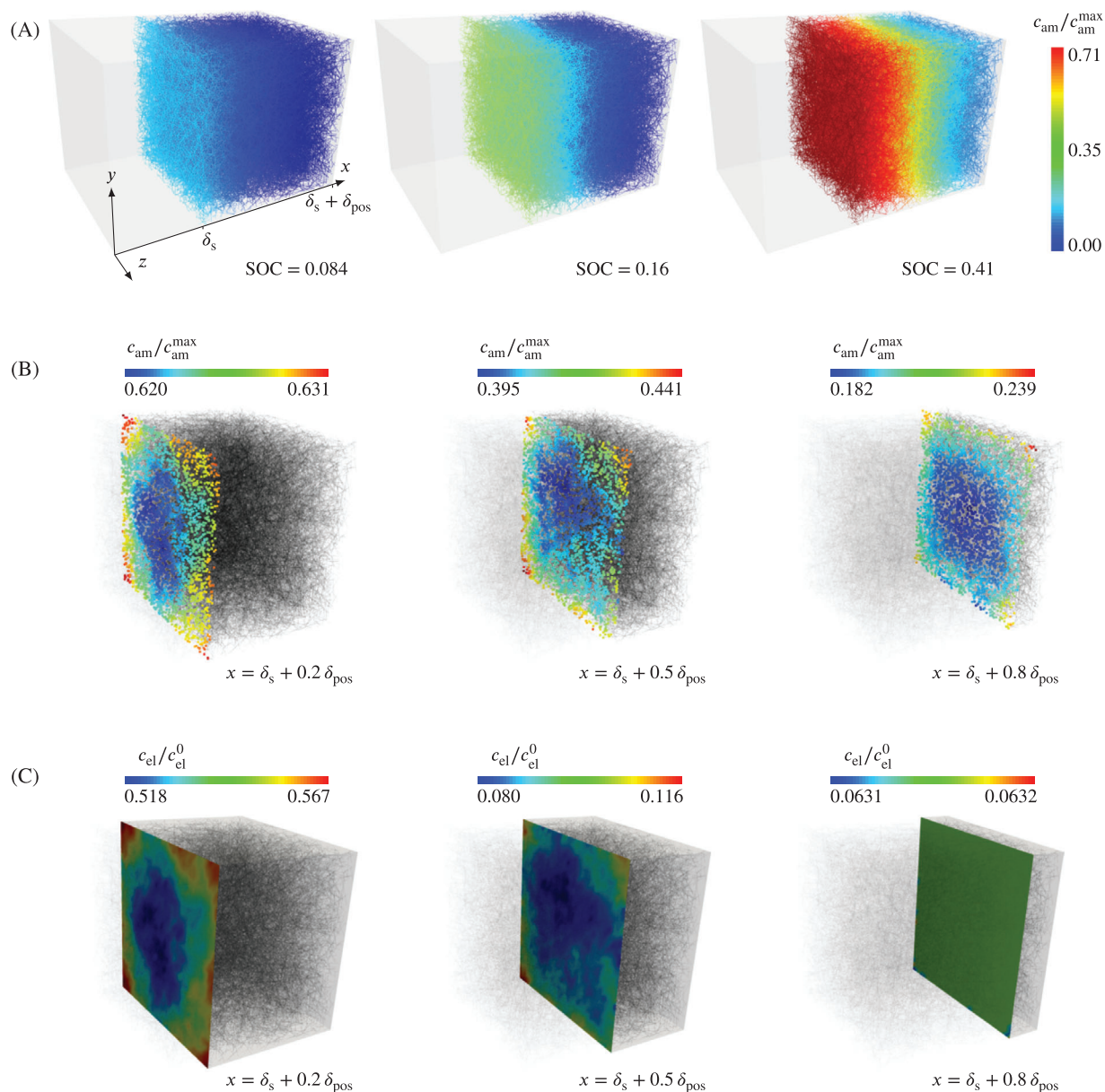
(A)

(B)

(C)

FIGURE 5 Contour plots of the positive electrode for $I = 10$ A m^{-2} discharge. (A) Concentration in the active fibers at SOC = 0.084, 0.16, and 0.41 (to be compared with the concentration profiles in Figure 7B). Concentration distributions on three yz-slices in the positive electrode (at $x = \delta_s + 0.2\,\delta_{pos}$, $\delta_s + 0.5\,\delta_{pos}$, and $\delta_s + 0.8\,\delta_{pos}$): (B) on the active fibers intersected by the planes, and (C) in the electrolyte. Each point in panel (B) represents a fiber cross-section. All the contour plots in panels (B) and (C) refer to SOC = 0.41. The results have been obtained with the finest discretization (20 elements for each fiber and $n_{msh} = 30$ for the electrolyte)

arrangement is not necessarily realistic, but it approximates the configuration investigated by Doyle et al.,[21] where a uniform distribution of particles was considered. For the purpose of this study, it was not deemed necessary to perform a statistical analysis and a single distribution of about 25,000 fibers in the positive electrode is considered representative. The fiber distribution is periodic in y and z directions: if a fiber crosses the external boundary of the domain the portion of fiber that falls out of the boundary is replicated at the opposite edge.

Initial and boundary conditions described in Sections 2.4 and 2.5, and further detailed in Section 5.1, are applied. We perform simulations with $I = 5$, 7, and 10 A m^{-2}, that is, within the 0.1–0.2 C rate range. The external surface of the positive electrode is insulated, that is, neither mass nor charge transfer across it.

The numerical simulations are performed using uniform discretizations: 10 equally sized segments for each fiber unless otherwise specified, and $n_{msh} \times n_{msh} \times n_{msh}$ eight-node hexahedral elements for the electrolyte domain. We perform simulations with $n_{msh} = 12$, 21, and 30, resulting in a number of nodes ranging between 250,000 and 280,000 in

the positive electrode. Emphasis is given to the presentation of results for $I = 10 \, \text{A m}^{-2}$ to provide a detailed comparison with the outcomes of Reference 21, where the distribution of local fields c_{el}, c_{am}, and $i_{\text{BV,am}}$ is shown exclusively for $I = 10 \, \text{A m}^{-2}$.

Substantial differences exist between the simulation settings by Doyle et al.[21] and our own. The differences lie in electrode microstructure and active material-electrolyte interaction modeling. Doyle et al.[21] focus on particle-based electrodes and their model is tailored for particles. They describe the electrolyte using a one-dimensional model where the microstructure associated to each electrode location x is represented through a single spherical particle. The particle-electrolyte interaction is described through the pore wall flux of lithium ions (j_n in the reference) which is assumed to be uniform on the particle surface. It turns out that the averaging procedure (from particle- to cell-scale) at the core of the pseudo-2D model used by Doyle et al.[21] makes the model insensitive to interaction between particles. We replace TiS$_2$ spherical inclusions with fiber-shaped inclusions (and this is justified by the use of TiS$_2$ nanotubes in battery applications[53,54]) and test a dimensionally reduced model tailored for fibers. A fiber is an elongated oriented object whose interaction with the surrounding electrolyte occurs over a broad region. The electric potential and concentration of the electrolyte in contact with the fiber depend on the location along the fiber-electrolyte interface. Concentration redistribution takes place along the fiber length too. The combination of these circumstances results in a nonuniform charge transfer along the fiber-electrolyte interface (refer to paragraph *Fiber-electrolyte charge transfer: Global response*), and in a range of fiber responses at a given x-location within the electrode Figure 5 (panels (B) and (C)). Furthermore, the electrochemical interaction between a fiber and the surrounding electrolyte affects the response of other fibers (more about this in Section 5.3).

Due to the differences just highlighted, a one-to-one match between our results and those by Doyle et al.[21] cannot realistically be expected. However, the work by Doyle et al.[21] is a good reference for multiple reasons. First, the reference solution is based on a half cell and thus the computational costs at the verification stage are halved compared to a full cell. Second, Doyle et al.[21] demonstrate that (radial) diffusion limitations in the active particles are negligible in their system, which is the assumption underlying the formulation of the dimensionally reduced model (Section 3). Third, Doyle et al.[21] report a comprehensive set of results, thus allowing to compare not just variables profiles, but also their trends. To the best of the author's knowledge, no reference solutions exists about local field distributions for battery electrodes with arbitrary arrangement of fibers. It follows that either a qualitative comparison is performed considering a different system (which is the case here), or a full-scale simulation of a fibrous electrode is performed to produce a reference solution (as the one in Section 5.1 which was performed for just one fiber). The latter option is excluded due to the very high computational cost.

With the numerical example at hand, we aim to show the capability of the proposed approach in dealing with fibrous electrodes where large amount of fibers are involved. Examples of target applications can be found in References 55 and 56. However, the results presented here are not necessarily representative of the actual response of realistic fibrous electrodes. For example, we match the 70% volume fraction used in Doyle et al.[21] for the sake of validation only. We are aware that achieving such a volume fraction of randomly distributed fibers is hardly possible in practical applications. Moreover, the prediction of the response of densely packed fiber ensembles and intersecting fibers would require ad-hoc formulation. The investigation of these and other aspects, which are critical to fibrous electrode design, falls beyond the scope of the current study.

Contour plots of the positive electrode are reported in Figure 5 for the numerical simulations performed with $I = 10 \, \text{A m}^{-2}$. Panel (A) shows the utilization of fibers at three stages of the discharge process (SOC = 0.084, 0.16, and 0.41). The progression of the utilization front is basically one-dimensional—from the separator ($x = \delta_{\text{s}}$) toward the rightmost edge of the positive electrode ($x = \delta_{\text{s}} + \delta_{\text{pos}}$)—but the concentration distribution is not strictly uniform on yz-planes at a given x-coordinate. This is evident from the cross-sections in panels (B) and (C) that refer to SOC = 0.41 and $x = \delta_{\text{s}} + 0.2 \, \delta_{\text{pos}}$, $\delta_{\text{s}} + 0.5 \, \delta_{\text{pos}}$, and $\delta_{\text{s}} + 0.8 \, \delta_{\text{pos}}$. The variability of the concentration in fibers intersected by the same cutting plane amounts to 0.06 $c_{\text{am}}^{\text{max}}$ at the most ($x = \delta_{\text{s}} + 0.8 \, \delta_{\text{pos}}$, panel (B)), while the variability of the concentration in the electrolyte on a given cross section amounts to 0.05 c_{el}^0 at the most ($x = \delta_{\text{s}} + 0.2 \, \delta_{\text{pos}}$, panel (C)). Apart from the visible role of the boundaries (boundary effect should however vanish by enlarging the simulation domain in x and y directions), local differences are appreciable also in the inner part of the cross section.

Lithium concentration in the electrolyte

Figure 5C shows that the concentration field is not uniform on a cross section. The variation is however modest, and it is therefore reasonable to assume the response along any line parallel to the x axis as equivalent for representation
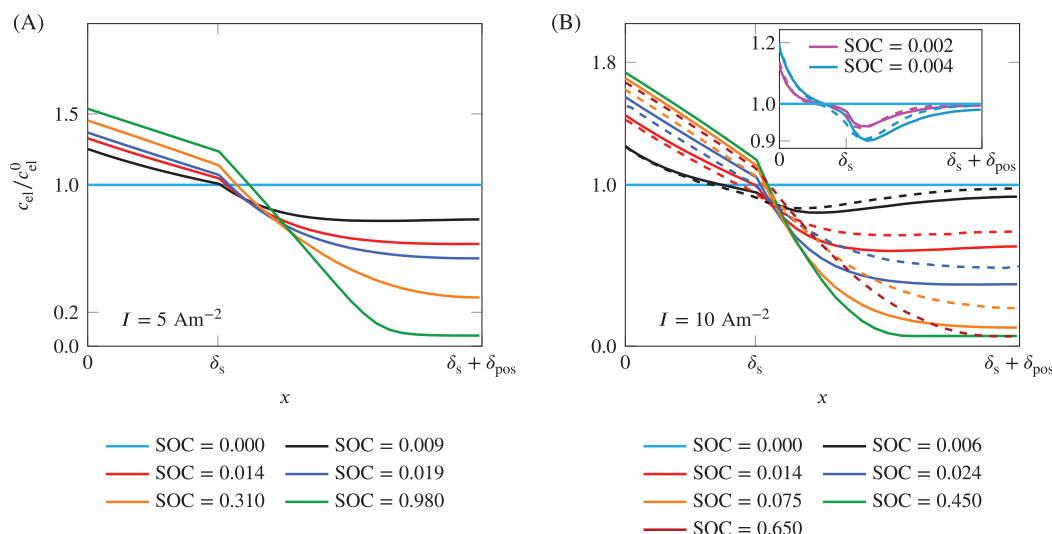
FIGURE 6 Concentration profiles within the electrolyte in the separator and positive electrode at various SOC with electric current densities (A) $I = 5$ A m^{-2} and (B) $I = 10$ A m^{-2}. The results refer to the finest discretization for the electrolyte domain ($n_{\mathrm{msh}} = 30$). Data have been extracted along the axis parallel to x-direction located at the center of yz-plane. The results by Doyle et al.[21] (their Figures 3 and 4) for $I = 10$ A m^{-2} at times $t = 10$, and 20 s (inset), and times $t = 50, 200, 400, 1400$, and 12,600 s (main plot) are reported with dashed lines in panel (B). The same color is used for our results and those of the reference when the SOC coincides

purposes. For convenience, data shown in Figure 6 have been sampled along the axial line of the half cell in the separator and electrode domain (the axial line passes through the center of the separator-electrode interface region and is parallel to the x axis).

The evolution patterns of the concentration profile are similar for $I = 5$ A m^{-2} (Figure 6A) and 10 A m^{-2} (Figure 6B): a linear distribution in the separator, then a rapid decrease at the separator-positive electrode interface $x = \delta_{\mathrm{s}}$ followed by a plateau. When $I = 5$ A m^{-2} the concentration gradient is modest and the depletion of the electrolyte ($c_{\mathrm{el}} \leq 0.07\, c_{\mathrm{el}}^0$) is attained in about 20% of the positive electrode thickness (region at the rightmost edge of the domain $x = \delta_{\mathrm{s}} + \delta_{\mathrm{pos}}$) by the end of the process (SOC = 0.98). A pronounced concentration gradient develops with $I = 10$ A m^{-2}, causing the depletion of the electrolyte ($c_{\mathrm{el}} \leq 0.07\, c_{\mathrm{el}}^0$) in roughly 50% of the electrode thickness at SOC = 0.45.

In Figure 6B, we report the results by Doyle et al.[21] for comparison. A good agreement is evident in the initial simulation steps; the concentration dip at the separator-positive electrode boundary is clearly captured (inset of Figure 6B). Concentration gradients and electrolyte depletion are more pronounced in the fibrous electrode at SOC > 0.006. Discrepancies in the overall evolution are attributable to the intrinsic differences (discussed above) between our simulation setting and that of the reference. The main difference between the fibrous and particle-based electrode simulations is that the first one stops at SOC = 0.45 (as it cannot proceed further), while the second proceeds up to about SOC = 0.83. A discussion about the causes of the early simulation interruption is postponed to paragraph *Fiber-electrolyte charge transfer: Global response*. Since Doyle et al.[21] report the electrolyte concentration profiles up to SOC = 0.65, this curve is shown as well in Figure 6B for completeness.

Lithium concentration in the fibers

Figure 7 shows the local utilization of the active material in the positive electrode for $I = 5$ A m^{-2} (Figure 7A) and 10 A m^{-2} (Figure 7B) in terms of the average concentration $\bar{c}_{\mathrm{am}}$ calculated as the mean fiber concentration on the electrode cross-sections orthogonal to the x-direction. For $I = 5$ A m^{-2}, the gradient of the utilization profile is modest. The variation of $\bar{c}_{\mathrm{am}}$ across the electrode is about $0.15\, c_{\mathrm{am}}^{\max}$ at the most, and the active material is fully exploited (up to SOC = 0.98, Figure 7A) by the end of the simulation. For $I = 10$ A m^{-2}, the active material utilization is
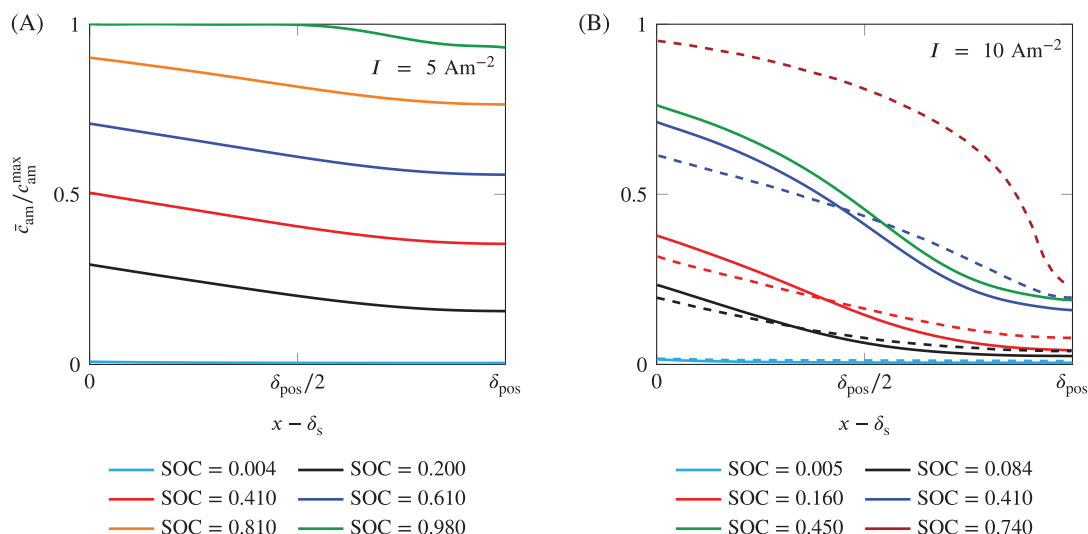
FIGURE 7 Concentration profiles within the active material in the positive electrode at various SOC for electric current densities (A) $I = 5$ A m^{-2} and (B) $I = 10$ A m^{-2}. The results refer to the finest discretization for the electrolyte domain ($n_{\mathrm{msh}} = 30$). On the vertical axis, we report the average concentration $\bar{c}_{\mathrm{am}}$ calculated over the electrode cross-sections orthogonal to the x-direction. The results by Doyle et al.[21] (their Figure 6) at times $t = 40, 1640, 3240, 8040$, and $14{,}400$ s are reported with dashed lines in panel (B). The same color is used for our results and those of the reference when the SOC coincides

nonuniform (Figure 7B): intense near the separator ($\bar{c}_{\mathrm{am}}/c_{\mathrm{am}}^{\max} \approx 0.76$ at the most at $x = \delta_{\mathrm{s}}$), and modest at the rightmost edge ($\bar{c}_{\mathrm{am}}/c_{\mathrm{am}}^{\max} \approx 0.18$ at the most at $x = \delta_{\mathrm{s}} + \delta_{\mathrm{pos}}$), with the difference between these two values that widens as the SOC increases. Our results (continuous lines in Figure 7B) qualitatively agree with those by Doyle et al.[21] (their Figure 6) up to SOC = 0.16: the two sets of results show modest differences up to SOC = 0.084 (black line), but show different patterns thereafter. At SOC = 0.41, the fibrous electrode is characterized by a higher utilization of the active material closer to the separator and a lower utilization of the active material at the rightmost edge of the domain compared to the particle-based electrode. In Figure 7B, we show both the utilization profile at the last stage of our simulation (SOC = 0.45) as well as the utilization profile at the last reported stage in the reference (SOC = 0.74).

Cell potential

Figure 8 shows the cell potential as a function of the SOC for $I = 5, 7$, and 10 A m^{-2} and for discretizations $n_{\mathrm{msh}} = 12, 21$, and 30. The active material utilization progressively reduces (the maximum achievable SOC reduces) as the discharge rate increases, in agreement with the results by Doyle et al.[21] Figure 8A shows that there are no appreciable differences between the results obtained with different meshes when $I = 5$ A m^{-2} is applied, suggesting that the converged solution is obtained with the coarsest mesh ($n_{\mathrm{msh}} = 12$). Similar arguments apply to the results obtained with $I = 7$ A m^{-2}. With $I = 10$ A m^{-2}, the results obtained with different n_{msh} overlap, but the maximum achievable SOC increases with n_{msh} (the maximum SOC is 0.36, 0.43, and 0.45 with $n_{\mathrm{msh}} = 12, 21$, and 30, respectively). Since a steeper concentration gradient develops in the electrolyte at higher rates (compare panel (A) with panel (B) in Figure 6), a proper representation of the cell response requires a finer mesh.

Numerical simulations are performed with time step Δt ranging between 1 and 20 s. We observe that the effect of the time step size on the outcome of the simulations is secondary compared to that of the spatial discretization, as differences between the results obtained with different time step setting are not appreciable in the discharge curve.

The results by Doyle et al.[21] for $I = 5$ and 10 A m^{-2} are reported in Figure 8B for comparison. The cell potential of the particle-based electrode exceeds that of the fibrous electrode with both $I = 5$ and 10 A m^{-2}. This is consistent with the comparison reported in Figures 6B and 7B. Figure 7B indeed shows that fibers near the separator are filled more quickly than particles and, at the same time, shortage of lithium at the rightmost edge of the cell ($x >$
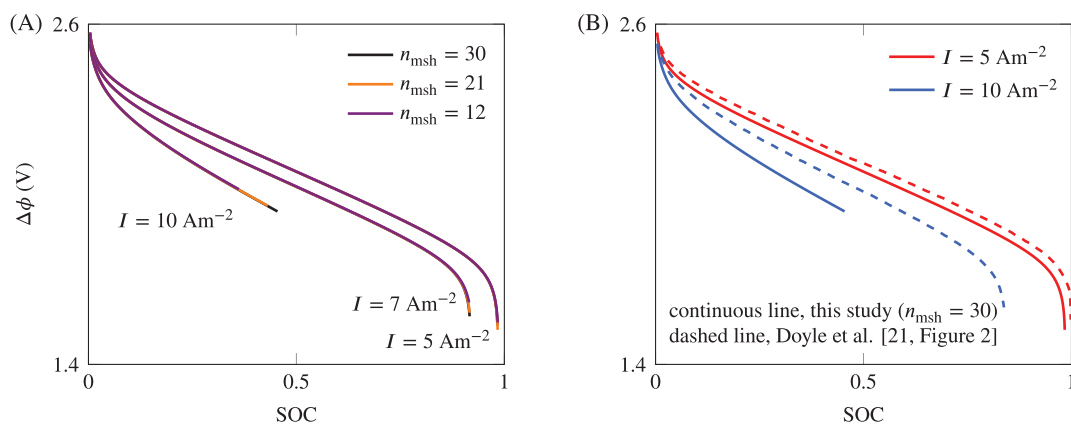
FIGURE 8 Discharge curve for galvanostatic discharge processes. (A) Mesh refinement study at $I = 5, 7$, and 10 A m^{-2}; simulations have been performed with structured meshes with $n_{\mathrm{msh}} = 12, 21$, and 30. (B) Comparison with the results by Doyle et al.[21] (their Figure 2) for $I = 5$ and 10 A m^{-2}
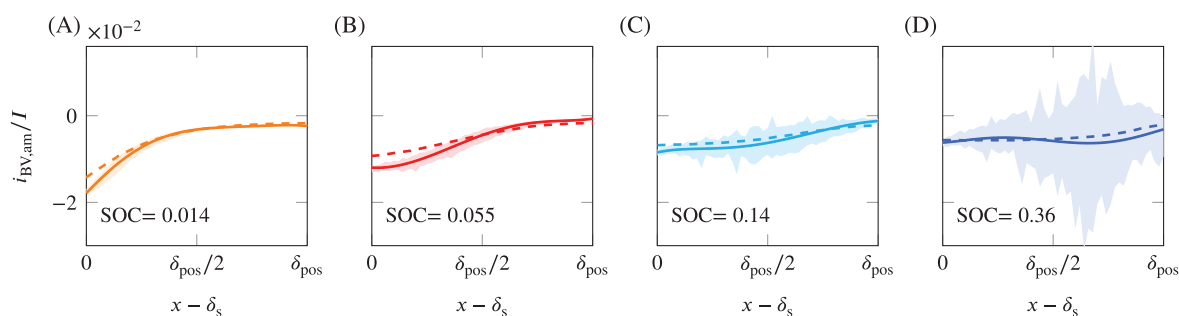

FIGURE 9 Charge transfer profiles for $I = 10$ A m^{-2} at four stages of the discharge process. Each point of the shaded regions represents the charge transfer averaged on the surface of a fiber and plotted at its midpoint. Solid lines represent the polynomial fits of the data. The results by Doyle et al.[21] (their Figure 5) at times $t = 200$ (SOC = 0.014), 1000 (SOC = 0.055), 2800 (SOC = 0.14), and 7000 s (SOC = 0.36) are reported as well (dashed lines)

$\delta_{\mathrm{s}} + \delta_{\mathrm{pos}}/2$) occurs earlier in the fibrous electrode (Figure 6). These circumstances concur to the accelerated reduction of the cell potential of the fibrous electrode (irrespective of the current applied) that ultimately results in a reduction of the active material utilization compared to the particle-based electrode. At $I = 10$ A m^{-2}, the ultimate SOC reduces from 0.83 to 0.45 switching from particle-based to fibrous electrode (this aspect is further discussed in the next paragraph).

Fiber-electrolyte charge transfer: Global response

To complete the validation of the dimensionally reduced model, Figure 9 shows the evolution of the charge transfer $i_{\mathrm{BV,am}}$ for 10 A m^{-2} and SOC between 0.014 to 0.36. The shaded regions represent the envelope plots of the charge transfer values sampled at the fiber discretization nodes. This compact representation shows the fluctuations of $i_{\mathrm{BV,am}}$ through the electrode thickness (i.e., along the x-direction) caused by the randomness of the fiber dispersion. The wider the shaded area the larger the spread of the exchange current over the electrode cross-section, to such an extent that the charge transfer changes sign at some location of the positive electrode, as Figure 9D shows. This is further discussed in the next paragraph (*Fiber-electrolyte charge transfer: Local response*). The polynomial fits of the data (solid lines) are shown to ease comparison against the results reported by Doyle et al.[21] in their Figure 5 (dashed lines).

The charge transfer distribution resulting from the dimensionally reduced model is (in average) in good agreement with the results of the pore wall flux reported by Doyle et al.[21] Even if the polynomial fits do not perfectly overlap with the reference solution, the overall evolution shows the same trend. The distinctive nature of the two approaches emerges from Figure 9. Since Doyle's model is based on a homogenization procedure, a single value of $i_{BV,am}$ is associated to a given x-coordinate. This is not the case for the dimensionally reduced model at hand. Since each fiber of the electrode is explicitly represented, the spreading of the charge transfer over yz cross-sections at given x is visible. Figure 9 shows that the extent of the variability of $i_{BV,am}$ is directly proportional to SOC, that is, when concentration gradients in electrolyte (Figure 6) and active material (Figure 7) are pronounced, the charge transfer is nonuniform at locations equidistant from the separator even if fibers are uniformly distributed within the electrode.

The progression of the active material utilization front (visible from Figure 5A) is apparent in Figure 9. At the beginning of the discharge process (panel (A)), lithium insertion into fibers occurs mainly at the leftmost edge of the electrode ($x = \delta_s$). As the process continues (panels (B) to (D)), fibers near the separator fill up and the reaction front shifts towards the body of the electrode. The transition is initially driven by the concentration-dependence of $U_{OC,am}$ (57), as a relatively small increase in fiber concentration has a large effect on the potential.[21] At a later stage, the intensification of charge transfer at the rightmost end of the electrode results in electrolyte depletion (Figure 6B), and transport limitations in the electrolyte become the most crucial aspect. Since the concentration-dependent conductivity approaches zero as c_{el} approaches 63 mol m^{-3} (definition of κ_{el} Table 6) the electric current approaches zero in 50% of the electrode thickness at SOC = 0.45 (refer to Equation (10) and Figure 6). It follows that 50% of the positive electrode (the portion at $x \geq \delta_s + 0.5\delta_{pos}$) is actually unavailable for lithiation at SOC = 0.45. The remaining portion of the positive electrode cannot sustain the lithium uptake necessary to fulfill boundary condition I and the simulation simply stops. This is evident from Figure 8, where the curve for $I = 10$ A m^{-2} is truncated at SOC = 0.45 and $\Delta\phi = 1.93$ V. A similar behavior is reported by Doyle et al.,[21] but at a higher discharge rate (their cell potential vs. SOC curve for $I = 20$ A m^{-2} is truncated at SOC = 0.3 and $\Delta\phi = 1.86$ V). We thus conclude that the time evolution of the field variables c_{el} (Figure 6B), c_{am} (Figure 7B), and $i_{BV,am}$ (Figure 9) and cell potential $\Delta\phi$ (Figure 8) predicted with the dimensionally reduced model show trends similar to those reported by Doyle et al.[21] The overall evolution of the system is consistent with the results reported by Doyle et al.,[21] but the insurgence of steep gradients within the positive electrode occurs at lower SOC. For example, Doyle et al.[21] determine electrolyte depletion in 10% of the particle-based electrode thickness at SOC = 0.65, while the dimensionally reduced model predicts electrolyte depletion in 50% of the fibrous electrode thickness at SOC = 0.45 (Figure 6B). Based on the (qualitative) comparisons conducted so far against the results by Doyle et al.[21] we believe that the approach is sound irrespective of the number of fibers (i.e., just one as in Section 5.1 or thousands as in this section).

Fiber-electrolyte charge transfer: Local response

The charge-transfer across the fiber-electrolyte interface is not uniform on the fiber boundary. Figure 10B shows the distribution of the charge transfer along the axis of the fibers highlighted in Figure 10A (SOC = 0.014). The distances between the midpoints of the fibers and the separator are approximately (1) $0.15\delta_{pos}$, (2) $0.30\delta_{pos}$, (3) $0.43\delta_{pos}$, and (4) $0.67\delta_{pos}$, with corresponding average values of $i_{BV,am}/I$ equal to (1) -1.1×10^{-2}, (2) -6.2×10^{-3}, (3) -3.9×10^{-3}, and (4) -2.4×10^{-3}, and average $i_{BV,am}$ values between -0.11 and -0.02 A m^{-2}. The response of the fibers is representative of the behavior of fibers located at the same distance from the separator, as evident from the comparison with Figure 9A (orange line).

The profiles shown in Figure 10B present a distinctive feature compared to those shown in Figure 2B (single-fiber investigation): $i_{BV,am}$ is positive in a portion of the fiber. The outcomes of the numerical simulations thus suggest that a local extraction of lithium takes place ($i_{BV,am} > 0$) while the boundary conditions promote lithium insertion ($i_{BV,am} < 0$). Before this aspect of the results is further discussed in Section 5.3, a few remarks are in order. First, the profiles shown in Figure 10B do not change by refining the fiber discretization, as we observed no appreciable differences between the results obtained with fibers discretized with 10 or 20 equally sized elements (the latter are reported in Figure 10B). Second, the shape of the profile is unaffected by the spatial orientation of the fibers (which is different for all of them). Third, the extent of the spikes at the tips reduces when the distance between fiber and separator increases, suggesting a dependence on the magnitude of the load experienced by the fiber. However, the applied current alone does not justify the steep gradient at the tips, because the loading conditions of the single fiber electrode in Section 5.1 are far more severe. Figure 2B shows that the average $i_{BV,am}$ ranges between -8.05 and -0.19 A m^{-2}. Since the most notable difference with the numerical
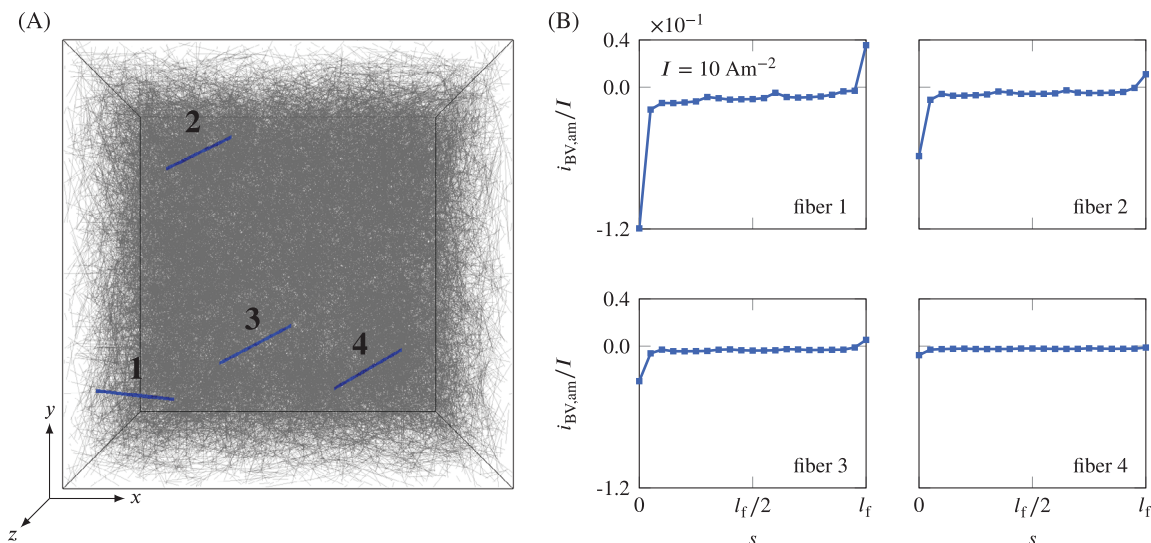
(A)

(B)

FIGURE 10 Charge transfer for $I = 10\,\mathrm{A\,m^{-2}}$. (A) Fibrous electrode geometry. (B) Charge transfer along the length of a selection of fibers at SOC = 0.014. Plots in panel (B) refer to the fibers highlighted in panel (A). The results have been obtained with the finest discretization (20 elements for each fiber domain and $n_{\mathrm{msh}} = 30$ for the electrolyte domain)

examples of Section 5.1 is the coexistence of multiple fibers, in the next section we focus on the effect of their mutual interaction.

5.3 | Charge transfer investigation

To the best of the authors' knowledge, there are no previous studies investigating the causes of a possible sign inversion of the charge transfer on the same active material inclusion (either from the mathematical or physical perspective). Even if an extensive study falls beyond the scope of this contribution, we aim to demonstrate that the gradients at the fiber tips and the sign inversion of $i_{\mathrm{BV,am}}$ reported in Figure 10 are not artifacts of the dimensionally reduced model. Indeed, the usage of the fully resolved model leads to the same results. To this end, we perform numerical simulations in a two-dimensional setting and focus on the battery cell configuration comprised of the positive electrode of Figure 1F into the half cell of Figure 1A. Both dimensionally reduced and fully resolved models are used. The cell is made of (i) a lithium plate of thickness $\delta_{\mathrm{neg}} = 20\,\mu\mathrm{m}$, (ii) a separator of thickness δ_{s} (we consider two values: $\delta_{\mathrm{s}} = 90$ and $45\,\mu\mathrm{m}$), and (iii) a positive electrode containing two elongated inclusions (we will refer to them as fibers, from now on) with their longest axis parallel to the x-direction. We restrict the simulated domain to the strip highlighted in yellow in Figure 1F. The thickness δ_{pos} of the positive electrode is such that $\delta_{\mathrm{s}} + \delta_{\mathrm{pos}} = 150\,\mu\mathrm{m}$, and the size of the simulation domain in the y direction is $L = 20\,\mu\mathrm{m}$.

We apply the initial and boundary conditions described in Sections 2.4 and 2.5. External surfaces other than the edge defined by $x = -\delta_{\mathrm{neg}}$ (refer to Figure 1F) are insulated. We perform simulations with electric current density $I = 15\,\mathrm{A\,m^{-2}}$, distance between fibers $\delta_{\mathrm{gap}} = 1\,\mu\mathrm{m}$, and a combination of parameter values (selected through a trial-error search) that allow the sign inversion of $i_{\mathrm{BV,am}}$ to manifest. Although very convenient from the modeling perspective, a combination of parameter values that cause the sign inversion of $i_{\mathrm{BV,am}}$ cannot be systematically identified using a setup with few fibers due to the large number of variables that come into play.

Operative constraints further complicate this analysis: on the one hand, the number of fibers must be limited in order to solve the problem with the fully resolved model; on the other hand, the active material volume fraction must be sufficiently high to allow concentration gradients to develop before the process terminates. For these reasons the length and thickness of fibers are set to $l_{\mathrm{f}} = 20\,\mu\mathrm{m}$ and $t_{\mathrm{f}} = 6\,\mu\mathrm{m}$, respectively, corresponding to $t_{\mathrm{f}}/L = 0.3$ and $l_{\mathrm{f}}/t_{\mathrm{f}} = 3.33$, that is, outside the range of values that guarantee the best match between dimensionally reduced and fully resolved models (Section 5.1). Note that the thickness t_{f} is used in place of diameter d_{f} due to the two-dimensional setting. Nevertheless, Figure 11 shows that the two approaches lead to the same pattern and that the sign inversion of $i_{\mathrm{BV,am}}$ emerges with both numerical approaches.
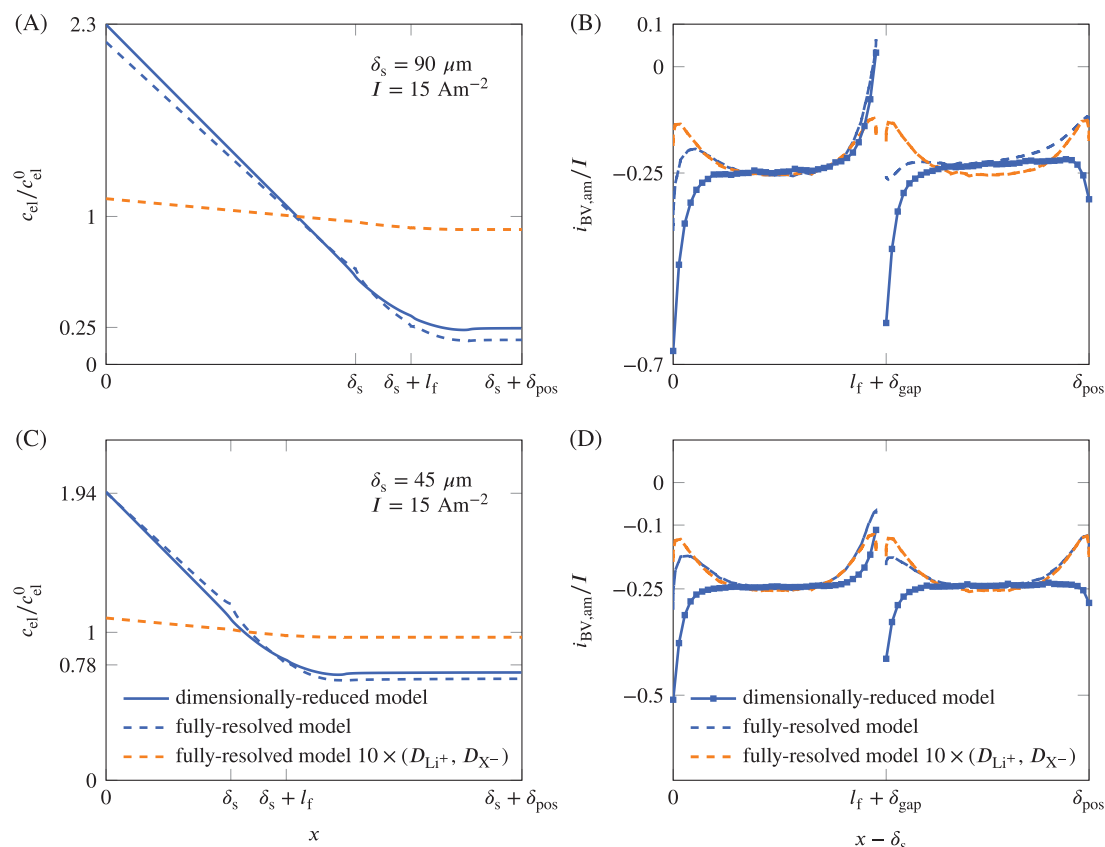
FIGURE 11 Electrolyte concentrations and interface currents for the two-fiber problem with fibers placed at two different locations in the electrolyte: far from the negative electrode (A, B) and close to the negative electrode (C, D). Due to the interaction between fibers, the current distribution around them is not uniform. The results predict a sign change close to the fiber tips when the fiber is far from the left electrode or where the electrolyte concentration is low. Similarly, choosing a higher diffusivity for the electrolyte results in a higher minimum concentration in the electrolyte and therefore positive currents are not observed. Results are shown at SOC ≈ 0.7 with an applied external current $I = 15 \, \mathrm{A \, m^{-2}}$

In the dimensionally reduced model simulations, 35 equally spaced segments are used for the discretization of each fiber, and about 51,000 bilinear quadrilateral elements are used for the discretization of separator and electrolyte in the positive electrode. In the fully resolved model simulations, we use a non-structured discretization of linear triangular elements (with about 2750 elements for both separator thicknesses). The number of elements of the dimensionally reduced model exceeds that of the fully resolved model because an unstructured mesh with a local refinement around fiber tips was used in the second case. In the fully resolved model simulations, the corners of the fibers are round-shaped (three-knots B-spline) to avoid current density concentration due to sharp edges (see, e.g., Reference 39). The results shown in Figure 11 have been obtained with the constitutive model described in Table 1 and with the material parameters listed in Tables 4 and 5 unless otherwise specified.

Figure 11 shows results at SOC ≈ 0.7 for separator thicknesses $\delta_s = 90$ and $45 \, \mu m$ obtained with dimensionally reduced (continuous lines) and fully resolved (dashed lines) models. Panels (A) and (C) shows the concentration profile in the electrolyte of the cell (separator and positive electrode) along the symmetry axis of the domain. The results of the dimensionally reduced model show also the profile at the fiber location in the electrolyte domain (recall that fiber and electrolyte meshes overlap in the dimensionally reduced model), while those of the fully resolved model show the profile along the fiber-electrolyte interface (data are ordered based on the x-coordinate). The pointwise difference between the two models is 10% at the most. Panels (B) and (D) shows the charge transfer profiles along the surface of the fibers. The fully resolved model profiles are roughly constant in the central portion of the fiber, and show local (global) maxima near (at) the fibers' ends, with sharp drops towards the tips with the exception of a few cases. The dimensionally reduced model profiles show a similar pattern but without local maxima. Differences are due to the low aspect ratio of fibers (and are consistent with the results reported in Figure 2B). The profiles obtained with the dimensionally reduced model for fiber 1 are identical to those shown in Figure 10B irrespective of the separator thickness. The steep gradient at the right tip of
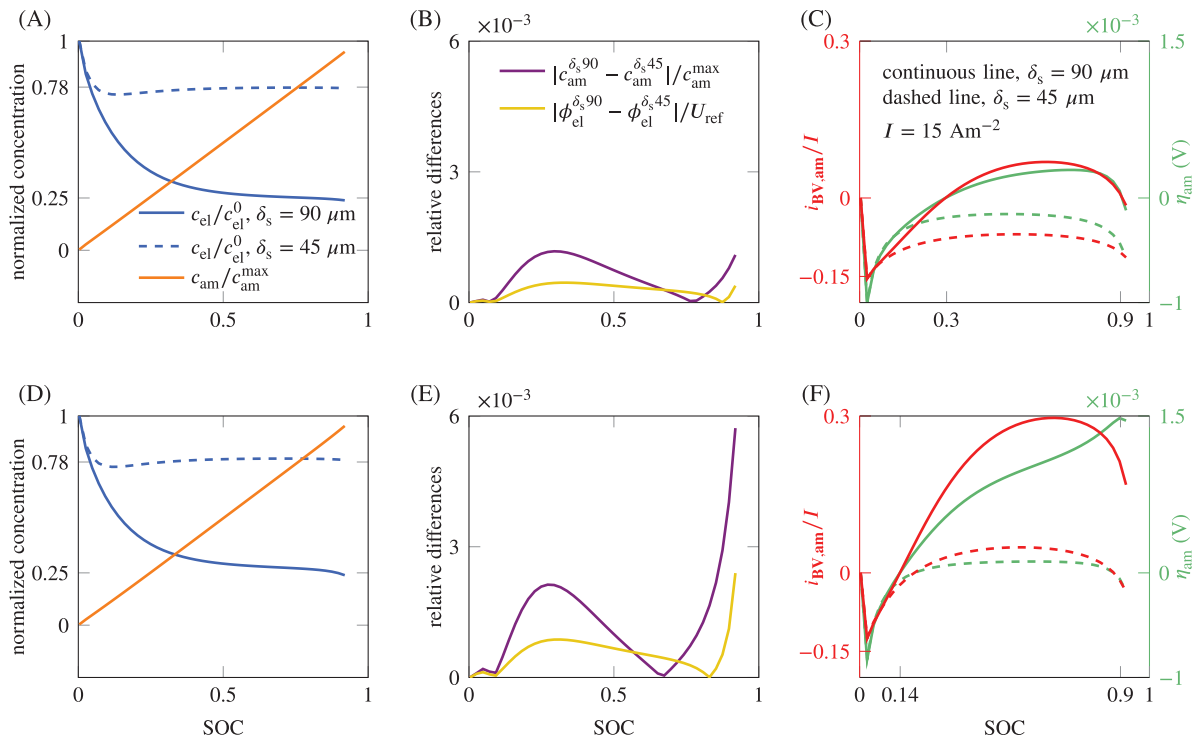
FIGURE 12 Comparison of the evolution of field variables at the right tip of fiber 1 ($x = \delta_s + l_f$ on the axial line, refer to Figure 1F) obtained with the fully resolved model for $\delta_s = 45$ and 90 μm: (A, D) concentration in electrolyte and fiber; (B, E) relative difference between the results in terms of fiber concentration c_{am} and electrolyte electric potential ϕ_{el}; and (C, F) charge transfer (8) or (13) and overpotential (14). Results in panels (A–C) have been obtained using the constitutive model described in Table 1 and with material parameters listed in Tables 4 and 5. Results in panels (D–F) have been obtained with the constitutive model described in Table 2 and material parameters listed in Tables 4 and 6

fiber 1 is visible also with the fully resolved model. Both approaches predict the sign inversion of $i_{BV,am}$ with $\delta_s = 90$ μm but not with $\delta_s = 45$ μm. Many factors contribute to the local distribution of $i_{BV,am}$. For example, Figure 11 shows that increasing D_{Li^+} and D_{X^-} by a factor of 10 (orange line) reduces the concentration gradient in the electrolyte and prevents the sign inversion of $i_{BV,am}$ for any of the considered values of δ_s.

We now discuss the factors that contribute to the sign inversion of $i_{BV,am}$ focusing on the evolution of the field variables at the location where $i_{BV,am}$ attains the largest positive value. Panels (A) to (C) report result obtained with the constitutive model described in Table 1 and with the material parameters listed in Tables 4 and 5 (the same setting that led to the results of Figure 11), while panels (D) to (F) report result obtained with the constitutive model described in Table 2 and with the material parameters listed in Tables 4 and 6. Figure 12 shows the evolution of field variables as a function of the SOC at the right tip of fiber 1 ($x = \delta_s + l_f$ on the axial line, i.e., at the fiber-electrolyte interface) for $\delta_s = 90$ and 45 μm. The results refer to the fully resolved model solution. Panel (A) shows the temporal counterpart of Figure 11 (panels (A) and (C) as well as the concentration evolution inside the fiber (orange line; we only report c_{am} for $\delta_s = 90$ μm because the deviation from the solution for $\delta_s = 45$ μm is not appreciable in this plot, as clarified by panel (B)). Panel (C) shows the temporal counterpart of Figure 11 (panels (B) and (D)). With $\delta_s = 90$ μm the charge transfer $i_{BV,am}$ is positive for most of the discharge process starting at SOC ≈ 0.3, while with $\delta_s = 45$ μm the charge transfer is always negative. The results reported in panel (D) are basically equivalent to those of panel (A), while those of panel (F) show that the sign inversion takes place with both geometrical setting when the constitutive models of Table 2 are used, even if the maximum value achieved is strongly reduced with $\delta_s = 45$ μm. These observations suggest that the sign inversion may manifest or not depending on the constitutive model used.

According to expression (8) (equivalently (13)), the sign inversion of $i_{BV,am}$ is determined by the surface overpotential η_{am} (14), being the exchange current density $i_{0,am}$ (56) non-negative by definition (exponents $\alpha_a = \alpha_c = 0.5$ in Table 4). The evolution of η_{am} ultimately depends on ϕ_{el} and c_{am} because of the assumed $\phi_{am} = 0$ (20) and definitions (14) and (57). Panel (B) shows that the instantaneous values of ϕ_{el} and c_{am} differ by 0.12% at the most

between the solutions for $\delta_s = 90$ and $45\ \mu m$ (the difference is up to 0.56% in panel (E)). Despite these small differences, the interplay between ϕ_{el} and c_{am} (through $U_{OC,am}$, (57)) results in a remarkably different evolution of η_{am} panel (C) and to a sign inversion with $\delta_s = 90$ but not with $45\ \mu m$. The values of c_{am} and c_{el} have an impact on the magnitude of $i_{BV,am}$ (8) through the exchange current density $i_{0,am}$ (56). These results agrees with the results presented by Gupta et al.[57] who performed an extensive sensitivity analysis to assess the influence of variables c_{am}, c_{el}, ϕ_{am}, and ϕ_{el} and their gradients on the charge transfer. Gupta et al.[57] conclude that the cross-interaction between c_{am}, ϕ_{am}, and ϕ_{el} determines the local charge transfer at the active material-electrolyte interface through the overpotential η.

With reference to the fully resolved model results shown in Figure 12, we add that a flux of lithium passing through fiber 1 takes place when $i_{BV,am} > 0$ in Figure 12 (panels (C) and (F) insertion takes place on the left tip and extraction at the right tip). The flux of ions in the electrolyte surrounding the fiber results in a gradient of the electric potential ϕ_{el} along the fiber-electrolyte interface. At the same time, lithium insertion into the fibers take place at different rates at different location of the same fiber, resulting in a nonuniform evolution of c_{am} and $U_{OC,am}$ along the fiber surface. This location-dependent evolution of fields ultimately result in a location-dependent evolution of the overpotential η_{am} along the fiber-electrolyte interface, thus inducing a flux of lithium through the fiber under certain circumstances.

In view of the discussion provided in this section, we conclude that the sign inversion of the charge transfer is not an artifact of the dimensionally reduced model as it can manifest with the fully resolved model too.

6 ⏐ CONCLUDING REMARKS

Structural batteries[10] inspired this work. A comprehensive modeling approach for such a multifunctional composite would require a coupled electrochemical-mechanical constitutive model. In this work, we focused on the electrochemical modeling and simulation of electrochemical processes in fibrous electrodes, neglecting mechanics and its coupling to electrochemistry. The focus is on the efficient modeling of the fibrous microstructure through a dimensionally reduced embedded fiber model and the corresponding constitutive model. We consider this a necessary first step towards the previously mentioned comprehensive modeling. The model, inspired by the embedded reinforcement model,[36] entails some simplifications. First, the distributions of field variables, namely electric potential and concentrations, are assumed to be spatially uniform, although temporally variable, at each fiber cross-section—this assumption makes the method suitable for high aspect ratio fibers in which fields are approximately uniform on the fiber cross-section. Second, electrochemical-mechanical coupling effects are neglected to simplify the formulation and limit the number of parameters—coupled electrochemical-mechanical effects are however known to affect battery cell performance[58] and might be extremely relevant in fiber electrodes for multifunctional applications.[7,42,59–61]

The proposed dimensionally reduced model ensures efficiency without sacrificing accuracy. The results presented in Sections 5.1 demonstrate that the accuracy of the dimensionally reduced model is comparable to that of the fully resolved model over a wide range of electrical loading conditions, and the agreement between the outcomes of the two approaches improves as the aspect ratio of the fibers increases. The dimensionally reduced model enables simple geometry discretization procedures and yields a remarkable reduction in the total number of degrees of freedom compared to the fully resolved model. In the example discussed in Section 5.1 the reduction amounts to 50% in terms of the discretization nodes for a single slender fiber with aspect ratio 60. We also show that the dimensionally reduced model is not competitive for relatively "thick" fibers, but those have to be considered as limit cases for which the dimensionally reduced model should not be used. While other aspects might influence the total simulation costs, the savings in terms of degrees of freedom are already evident with a single fiber, and it is reasonable to speculate that they increase with volume fraction and slenderness of the fibers. This makes the dimensionally reduced model inherently suitable for three-dimensional numerical simulations of nanowire electrodes that would otherwise be quite costly to perform using conformal meshing techniques[12,15] (the electrodes simulated in Section 5.2 contain up to 25,000 fiber, corresponding to a volume fraction of 70% of active material). We further show that the results are consistent with those obtained with the porous-electrode theory if equivalent microstructures—equivalent in terms of porosity—are considered. The dimensionally reduced model is, therefore, a valuable alternative to the fully resolved model for the modeling and simulations of battery electrodes comprised of high aspect ratio one-dimensional active

materials whose diameter is orders of magnitude smaller than the thickness of the electrode. Nanowire battery electrodes and fibrous multifunctional electrodes with high volume fractions of active materials are therefore suitable applications.

In view of the investigation described in Section 5.3, we conclude that interactions between active material fibers affect the solution fields' local distribution and can determine the sign inversion of the charge transfer $i_{BV,am}$ (extraction in place of insertion) in part of the fiber surface. This effect is further amplified if the distance between fibers is of the same order as the characteristic size of the fibers (or smaller). An investigation about the physical meaning of the sign inversion of $i_{BV,am}$ is beyond the scope of this study. We do however stress that when two fibers are close to each other, as in Section 5.3, the results of the dimensionally reduced model are consistent with those of the fully resolved model, as the sign inversion of $i_{BV,am}$ is present in both. This suggests that the sign inversion of the charge transfer is an intrinsic feature of the governing equations; a feature that manifests itself under special conditions (combination of constitutive model, geometry, material parameters, and boundary conditions) and cannot be therefore considered an artifact of the approximations introduced in the development of model.

DATA AVAILABILITY STATEMENT
The data that support the findings of this study are available from the corresponding author upon request.

ORCID
Mohsen Goudarzi https://orcid.org/0000-0002-7321-3432
Davide Grazioli https://orcid.org/0000-0003-2495-1508
Angelo Simone https://orcid.org/0000-0001-9726-0068

REFERENCES
1. Pampal ES, Stojanovska E, Simon B, Kilic A. A review of nanofibrous structures in lithium ion batteries. *J Power Sources*. 2015;300:199-215.
2. Jung JW, Lee CL, Yu S, Kim ID. Electrospun nanofibers as a platform for advanced secondary batteries: a comprehensive review. *J Mater Chem A*. 2016;4:703-750.
3. Li W, Zeng L, Wu Y, Yu Y. Nanostructured electrode materials for lithium-ion and sodium-ion batteries via electrospinning. *Sci China Mater*. 2016;59(4):287-321.
4. Lu L, Hu Y, Dai K. The advance of fiber-shaped lithium ion batteries. *Mater Today Chem*. 2017;5:24-33.
5. Wang L, Yu Y, Chen PC, Chen CH. Electrospun carbon–cobalt composite nanofiber as an anode material for lithium ion batteries. *Scr Mater*. 2008;58(5):405-408.
6. Asp LE, Johansson MKG, Lindbergh G, Xu J, Zenkert D. Structural battery composites: a review. *Funct Compos Struct*. 2019;1(4):042001.
7. Asp LE, Bouton K, Carlstedt D, et al. A structural battery and its multifunctional performance. *Adv Energy Sustain Res*. 2021;2:2000093.
8. Asp LE. Multifunctional composite materials for energy storage in structural load paths. *Plast Rubber Compos*. 2013;42(4):144-149.
9. Ekstedt S, Wysocki M, Asp L. Structural batteries made from fibre reinforced composites. *Plast Rubber Compos*. 2010;3(4/5):148-150.
10. Liu P, Sherman E, Jacobsen A. Design and fabrication of multifunctional structural batteries. *J Power Sources*. 2009;189(1):646-650.
11. Trembacki BL, Noble DR, Brunini VE, Ferraro ME, Roberts SA. Mesoscale effective property simulations incorporating conductive binder. *J Electrochem Soc*. 2017;164(11):E3613-E3626.
12. Roberts SA, Mendoza H, Brunini VE, Noble DR. A verified conformal decomposition finite element method for implicit, many-material geometries. *J Comput Phys*. 2018;375:352-367.
13. Ferraro ME, Trembacki BL, Brunini VE, Noble DR, Roberts SA. Electrode mesoscale as a collection of particles: coupled electrochemical and mechanical analysis of NMC cathodes. *J Electrochem Soc*. 2020;167(1):013543.
14. Mai W, Yang M, Soghrati S. A particle-resolved 3D finite element model to study the effect of cathode microstructure on the behavior of lithium ion batteries. *Electrochim Acta*. 2019;294:192-209.

15. Liang B, Nagarajan A, Soghrati S. Scalable parallel implementation of CISAMR: a non-iterative mesh generation algorithm. *Comput Mech*. 2018;64(1):173-195.

16. Liang B, Nagarajan A, Ahmadian H, Soghrati S. Analyzing effects of surface roughness, voids, and particle–matrix interfacial bonding on the failure response of a heterogeneous adhesive. *Comput Methods Appl Mech Eng*. 2019;346:410-439.

17. Pai S, Kwon J, Liang B, Cho H, Soghrati S. Finite element analysis of the impact of bone nanostructure on its piezoelectric response. *Biomech Model Mechanobiol*. 2021;20:1689-1708.

18. Lv T, Yao Y, Li N, Chen T. Wearable fiber-shaped energy conversion and storage devices based on aligned carbon nanotubes. *Nano Today*. 2016;11(5):644-660.

19. Persano L, Camposeo A, Tekmen C, Pisignano D. Industrial upscaling of electrospinning and applications of polymer nanofibers: a review. *Macromol Mater Eng*. 2013;298(5):504-520.

20. Liberale F, Fiore M, Ruffo R, Bernasconi R, Shiratori S, Magagnin L. Red phosphorus decorated electrospun carbon anodes for high efficiency lithium ion batteries. *Sci Rep*. 2020;10(1):13233.

21. Doyle M, Fuller TF, Newman J. Modeling of galvanostatic charge and discharge of the lithium/polymer/insertion cell. *J Electrochem Soc*. 1993;140(6):1526-1533.

22. Franco AA. Multiscale modelling and numerical simulation of rechargeable lithium ion batteries: Concepts, methods and challenges. *RSC Adv*. 2013;3(32):13027.

23. Grazioli D, Magri M, Salvadori A. Computational modeling of Li-ion batteries. *Comput Mech*. 2016;58(6):889-909.

24. Zhang D, Bertei A, Tariq F, Brandon N, Cai Q. Progress in 3D electrode microstructure modelling for fuel cells and batteries: transport and electrochemical performance. *Progress Energy*. 2019;1(1):012003.

25. Zhao Y, Stein P, Bai Y, Al-Siraj M, Yang Y, Xu BX. A review on modeling of electro-chemo-mechanics in lithium-ion batteries. *J Power Sources*. 2019;413:259-283.

26. Franco AA, Rucci A, Brandell D, et al. Boosting rechargeable batteries R&D by multiscale modeling: myth or reality? *Chem Rev*. 2019;119(7):4569-4627.

27. Xu J, Lindbergh G, Varna J. Carbon fiber composites with battery function: stresses and dimensional changes due to Li-ion diffusion. *J Compos Mater*. 2018;52(20):2729-2742.

28. Carlstedt D, Runesson K, Larsson F, Xu J, Asp LE. Electro-chemo-mechanically coupled computational modelling of structural batteries. *Multifunct Mater*. 2020;3(4):045002.

29. Fang R, Farah P, Popp A, Wall WA. A monolithic, mortar-based interface coupling and solution scheme for finite element simulations of lithium-ion cells. *Int J Numer Methods Eng*. 2018;114(13):1411-1437.

30. Zhuo M, Grazioli D, Simone A. Active material utilization and capacity of fiber-based battery electrodes. *Electrochim Acta*. 2020;333:134929.

31. Chen L, He YL, Tao WQ, Zelenay P, Mukundan R, Kang Q. Pore-scale study of multiphase reactive transport in fibrous electrodes of vanadium redox flow batteries. *Electrochim Acta*. 2017;248:425-439.

32. Zhang D, Cai Q, Taiwo OO, Yufit V, Brandon NP, Gu S. The effect of wetting area in carbon paper electrode on the performance of vanadium redox flow batteries: a three-dimensional lattice Boltzmann study. *Electrochim Acta*. 2018;283:1806-1819.

33. Zhang D, Forner-Cuenca A, Taiwo OO, et al. Understanding the role of the porous electrode microstructure in redox flow battery performance using an experimentally validated 3D pore-scale lattice Boltzmann model. *J Power Sources*. 2020;447:227249.

34. Goudarzi M, Simone A. Discrete inclusion models for reinforced composites: Comparative performance analysis and modeling challenges. *Comput Methods Appl Mech Eng*. 2019;355:535-557.

35. Goudarzi M, Simone A. Fiber neutrality in fiber-reinforced composites: Evidence from a computational study. *Int J Solids*. 2019;156:14-28.

36. Balakrishnan S, Murray DW. Finite Element Prediction of Reinforced Concrete Behavior. Structural Engineering Report no. 138, Department of Civil Engineering, The University of Alberta; Edmonton, Alberta, Canada; 1986.

37. Newman J, Thomas-Alyea KE. *Electrochemical Systems*. 3rd ed. John Wiley and Sons; 2004.

38. Grazioli D, Verners O, Zadin V, Brandell D, Simone A. Electrochemical-mechanical modeling of solid polymer electrolytes: impact of mechanical stresses on Li-ion battery performance. *Electrochim Acta*. 2019;296:1122-1141.

39. Grazioli D, Zadin V, Brandell D, Simone A. Electrochemical-mechanical modeling of solid polymer electrolytes: stress development and non-uniform electric current density in trench geometry microbatteries. *Electrochim Acta*. 2019;296:1142-1162.

40. Grillet AM, Humplik T, Stirrup EK, et al. Conductivity degradation of polyvinylidene fluoride composite binder during cycling: measurements and simulations for lithium-ion batteries. *J Electrochem Soc*. 2016;163(9):A1859-A1871.

41. Purkayastha RT, McMeeking RM. An integrated 2-D model of a lithium ion battery: the effect of material parameters and morphology on storage particle stress. *Comput Mech*. 2012;50(2):209-227.

42. Jacques E, Kjell MH, Zenkert D, Lindbergh G, Behm M. Expansion of carbon fibres induced by lithium intercalation for structural electrode applications. *Carbon*. 2013;59:246-254.

43. Newman J, Tiedemann W. Porous-electrode theory with battery applications. *AICHE J*. 1975;21(1):25-41.

44. Salvadori A, Grazioli D, Geers MGD, Danilov D, Notten PHL. A multiscale-compatible approach in modeling ionic transport in the electrolyte of (lithium ion) batteries. *J Power Sources*. 2015;293:892-911.

45. Salvadori A, Grazioli D, Magri M, Geers MGD, Danilov D, Notten PHL. On the role of saturation in modeling ionic transport in the electrolyte of (lithium ion) batteries. *J Power Sources*. 2015;294:696-710.

46. de Souza Neto EA, Peric D, Owen DR. *Computational Methods for Plasticity*. 1st ed. Wiley; 2014.

47. Goudarzi M, Geijselaers HJM, Akkerman R. Efficient analysis of dense fiber reinforcement using a reduced embedded formulation. *Comput Mech*. 2021;67:1-15.

48. Golmon S, Maute K, Dunn ML. Numerical modeling of electrochemical-mechanical interactions in lithium polymer batteries. *Comput Struct*. 2009;87(23):1567-1579.

49. Xu W, Wang J, Ding F, et al. Lithium metal anodes for rechargeable batteries. *Energy Environ Sci*. 2014;7(2):513-537.

50. Doyle CM. *Design and Simulation of Lithium Rechargeable Batteries*. PhD thesis. Lawrence Berkeley National Laboratory, California; 1995.

51. Newman J. Dualfoil: Program for lithium ion, sodium ion, and nickel-metal hydride battery simulation; 1998. Accessed June 20, 2021. http://www.cchem.berkeley.edu/jsngrp/fortran.html

52. Widom B. Random sequential addition of hard spheres to a volume. *J Chem Phys*. 1966;44(10):3888-3894.

53. Chen J, Tao ZL, Li SL. Lithium intercalation in open-ended TiS2 nanotubes. *Angew Chem Int Ed*. 2003;42(19):2147-2151.

54. Li SN, Liu JB, Liu BX. First principles study of nanostructured TiS_2 electrodes for Na and Mg ion storage. *J Power Sources*. 2016;320:322-331.

55. Aravindan V, Sundaramurthy J, Kumar PS, et al. A novel strategy to construct high performance lithium-ion cells using one dimensional electrospun nanofibers, electrodes and separators. *Nanoscale*. 2013;5:10636-10645.

56. Jayaraman S, Aravindan V, Kumar PS, Ling WC, Ramakrishna S, Madhavi S. Exceptional performance of $TiNb_2O_7$ anode in all one-dimensional architecture by electrospinning. *ACS Appl Mater Interf*. 2014;6:8660-8666.

57. Gupta A, Seo JH, Zhang X, Du W, Sastry AM, Shyy W. Effective transport properties of $LiMn_2O_4$ electrode via particle-scale modeling. *J Electrochem Soc*. 2011;158(5):A487-A497.

58. Mukhopadhyay A, Sheldon BW. Deformation and stress in electrode materials for Li-ion batteries. *Prog Mater Sci*. 2014;63:58-116.

59. Snyder JF, Wong EL, Hubbard CW. Evaluation of commercially available carbon fibers, fabrics, and papers for potential use in multifunctional energy storage applications. *J Electrochem Soc*. 2009;156(3):A215.

60. Kim HC, Sastry AM. Effects of carbon fiber electrode deformation in multifunctional structural lithium ion batteries. *J Intell Mater Syst Struct*. 2012;23(16):1787-1797.

61. Jacques E, Kjell MH, Zenkert D, Lindbergh G, Behm M, Willgert M. Impact of electrochemical cycling on the tensile properties of carbon fibres for structural lithium-ion composite batteries. *Compos Sci Technol*. 2012;72(7):792-798.